Refined sub-region nanoindentation and FEM modeling of solvent-modified sintered silver joints for enhanced reliability prediction in power electronics

Wang, Xinyue; Bian, Letao; Yang, Zhoudong; Chen, Haixue; Sun, Yiping; Liu, Wenting; Zhang, Guoqi; Zhang, Jing; Liu, Pan

DOI
10.1016/j.matdes.2025.114716

Publication date
2025

Document Version
Final published version

Published in
Materials and Design

Materials & Design 259 (2025) 114716

Contents lists available at ScienceDirect

Materials & Design

journal homepage: www.elsevier.com/locate/matdes

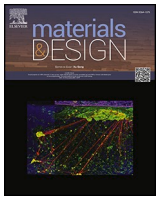

Refined sub-region nanoindentation and FEM modeling of solvent-modified sintered silver joints for enhanced reliability prediction in power electronics☆

Xinyue Wang [a], Letao Bian [a], Zhoudong Yang [a], Haixue Chen [a], Yiping Sun [a], Wenting Liu [a], Guoqi Zhang [b], Jing Zhang [c], Pan Liu [a,d,*]

[a] College of Intelligent Robotics and Advanced Manufacturing, Fudan University, Shanghai 200433, China
[b] Department of Microelectronics, Delft University of Technology, 2628 CD Delft, the Netherlands
[c] Heraeus Materials Technology Shanghai Ltd., Shanghai 201108, China
[d] Research Institute of Fudan University in Ningbo, Zhejiang Province 315336, China

ARTICLE INFO

Keywords:
Sub-region modeling
Nanoindentation
FEM simulation
Pressureless sintered silver
Solvent modification
Power electronics packaging

ABSTRACT

The mechanical reliability of sintered silver joints, widely used in power electronics packaging, is critical for long-term applications such as electric vehicle converters. However, conventional homogeneous modeling often oversimplifies internal microstructural variations and limits the accuracy of stress prediction, especially under thermal cycling. In this study, a region-refined modeling framework is proposed to account for epoxy-regulated porosity and mechanical inhomogeneity across the joint. Pressureless die-attach joints were prepared using submicron silver pastes with varying epoxy contents (0~4 wt%). The joint was divided into five sub-regions from the center to the fillet for localized characterization. Nanoindentation, SEM, and EDS analyses were conducted to assess region-specific mechanical properties and microstructure. Power-law constitutive models were extracted for each region and implemented into finite element simulations of thermal cycling (−55 ~ 150 °C, 2 cycles/h, 250 h). The sub-region FEM model more accurately captured local stress concentrations and identified failure-prone areas, particularly near the fillet, compared to conventional homogeneous models. Experimental validation confirmed a good correlation between simulated stress zones and observed degradation. This sub-region strategy provides a robust framework for reliability prediction and design optimization of sintered silver joints in high-performance, large-area packaging applications.

1. Introduction

With the increasing demand for operating at elevated temperatures, higher switching frequencies, and greater power densities, interconnect materials for power electronics packaging face increasing demands for improved thermal and electrical conductivities, low creep rates, and robust thermo-mechanical stability [1–3]. Sintered silver, as a benchmark die-attach material for the next-generation power electronics, has been applied as die-attach and heatsink attach solutions for wide bandgap (WBG) semiconductors such as SiC and GaN [4–6]. As an interconnect solution alternative to conventional solder alloys, it not only offers superior thermal, electrical, and mechanical properties, but also enables low-temperature processes such as the pressureless sintering [7–10].

The mechanical integrity of the die-attach layer plays a decisive role in the reliability of power modules [5,11]. Sintered joints must withstand repeated and extended thermal cycling resulting from power on/off operations or ambient temperature fluctuations, typically ranging from −55 °C to 150 °C in standard reliability qualification tests (e.g., JEDEC JESD22-A104D) [12,13]. Under such conditions, silver joints are exposed to cyclic mismatches in thermal expansion with adjacent materials such as silicon chips, metallization layers, and ceramic substrates [14,15]. These mismatches induce shear and normal stresses, which accumulate over time, eventually initiating cracks, delamination, or interfacial debonding that compromise device performance or trigger catastrophic failure [15–17].

☆ This article is part of a special issue entitled: 'Nanomechanical Testing 2024' published in Materials & Design.

* Corresponding author at: College of Intelligent Robotics and Advanced Manufacturing, Fudan University, Shanghai 200433, China.
E-mail address: panliu@fudan.edu.cn (P. Liu).

https://doi.org/10.1016/j.matdes.2025.114716
Received 30 May 2025; Received in revised form 8 August 2025; Accepted 7 September 2025
Available online 9 September 2025

Therefore, sintered silver joints frequently experience thermo-mechanical degradation during long-term service [18]. For better evaluation of the thermal–mechanical degradation, the finite element method (FEM) is commonly applied. However, most FEM simulations with sintered silver are facing critical challenges. Firstly, the material properties are insufficient for such a porous material [19]. For an accurate FEM simulation for electronics packaging reliability, material properties such as thermal conductivity, CTE, and elastic modulus are essential, while highly dependent on the material's composition, processing conditions, and testing methodology [20]. Especially in multi-domain FEM simulations, the constitutive behavior of sintered joints is highly sensitive to porosity, which typically ranges from below 10 % in pressure-assisted systems to 10∼35 % or more in pressureless sintered joints. The higher residual porosity in pressureless sintering introduces considerable heterogeneity, making accurate mechanical modeling particularly challenging [21]. Secondly, most FEM simulations used in reliability assessments assume the joint material is homogeneous and isotropic with constant elastic–plastic properties [22]. Though such simplification enables rapid simulation, it evidently deviates from the actual material conditions. In practice, sintered silver joints exhibit substantial microstructural heterogeneity due to factors such as powder size distribution, solvent evaporation rate, sintering temperature gradient, and the non-uniform distribution of resin-based additives [17,23–25]. These factors contribute to spatial variations in porosity, grain coarsening, local densification, and residual stress fields, all of which strongly influence the local mechanical response. This is particularly evident in pressureless sintering, where the absence of external pressure commonly promotes fillet formation surrounding the chip edges. Critically, regions near the joint fillet and chip periphery typically exhibit higher porosity and reduced mechanical integrity due to incomplete densification and stress concentration effects [26]. These localized inhomogeneities give rise to spatially dependent stiffness and strength properties, which cannot be accurately captured using bulk-averaged parameters. As a result, conventional homogeneous models tend to underestimate the stress intensity factors, particularly at crack-prone interfaces, which are insufficient to predict the early-stage failures.

Recent advances in instrumentation have enabled spatially resolved mechanical property characterization at the microscale [27–30]. In particular, nanoindentation techniques now enable detailed mapping of hardness and elastic modulus with sub-micron spatial resolution across the joint cross-section [31–34]. This creates opportunities for constructing sub-region-specific constitutive models that reflect the actual micro-mechanical landscape of the sintered structure [12,35]. By integrating these localized models into FEM simulations, it becomes feasible to capture more realistic stress gradients and predict the evolution of thermomechanical damage with greater fidelity.

Meanwhile, the introduction of epoxy additives into silver pastes offers additional opportunities to tune the joint performance [36,37]. These organic modifiers, commonly used at concentrations of 0∼10 wt %, directly impact the rheology of pastes, kinetics of sintering, and the porosity distribution after sintering [13]. Epoxy additives at proper content enhance the joint integrity by promoting uniform densification and improving adhesion at the joint interface. However, excessive epoxy content may leave carbon-rich residues to compromise the thermal conductivity, necessitating a balance between the mechanical reinforcement and the thermal/electrical functionality [38]. Although epoxy additives' global effects are known, their influence on spatial microstructural variations and local mechanical characteristics remains insufficiently studied. In particular, there is a lack of spatially resolved investigations that directly link epoxy content to local property gradients. The consequences of these gradients on thermal stress distribution during cyclic loading require further investigation.

To address the aforementioned limitations, this work proposes a refined sub-region modeling framework that integrates localized nanoindentation-based mechanical characterization with FEM stress simulations. As outlined in Fig. 1, submicron silver pastes with varying epoxy contents (0∼4 wt%) were formulated through solvent regulation and sintered under pressureless conditions to obtain joint samples. Based on shear strength as the primary criterion, Ag-2 and Ag-0 were selected as the optimized and reference samples, respectively, for further characterization and investigation. Detailed SEM/EDS analyses were employed to assess porosity and elemental distribution across five defined sub-regions, while nanoindentation testing quantified spatial variations in hardness and modulus. Region-specific power-law constitutive models were extracted and incorporated into FEM simulations to evaluate thermal stress distribution under cyclic loading. Compared with conventional homogeneous models, the sub-region approach demonstrated a better agreement with experimental thermal cycling test (TCT) results, particularly in identifying high-risk stress zones near the fillet. This study provides a predictive and design-oriented methodology to guide material formulation and joint structure optimization for reliable high-performance power electronics.

2. Materials and methodology

2.1. Preparation of epoxy-modified Ag pastes and sintered samples

A series of five submicron pressureless sintering silver pastes (Ag-0 to Ag-4) were formulated using uniformly dispersed silver particles and customized organic binders. The silver powder used (provided by Ningbo Guangbo Nano New Materials Co., Ltd.) exhibited a near-spherical morphology with an average particle size around 500 nm, as shown in Fig. 2a.

The solvent and resin system was tailored to regulate rheology and cure characteristics. Terpineol (T) and polyethylene glycol (PEG), mixed in a 1:2 mass ratio, served as dispersion media to improve particle wetting and stability. The epoxy matrix consisted of bisphenol A resin (YD) and methyl tetrahydrophthalic anhydride (WNY-1021) in a 10:9 ratio, with 2-ethyl-4-methylimidazole (EMI-2,4) added as a latent accelerator (WNY-1021: EMI-2,4 = 10:1 by weight). The specific composition of the solvent-regulated epoxy-based Ag sintering pastes designed in this work is shown in Table 1. These were mixed with silver powder (85 wt%) and processed using a high-speed planetary mixer at 1000 rpm for 3min to ensure homogeneous distribution.

The formulated pastes were deposited on substrates via stencil printing or precision dispensing (Musashi 350PC Smart Dispenser), depending on the application geometry. For die-attach samples, Ag-metallized silicon dummy chips (4 mm × 4 mm × 0.32 mm) were bonded onto ceramic substrates using a Datacon 2200 evo system. As shown in Fig. 2c, two types of specimens were fabricated, including actual die-attach joints for reliability and microstructural studies, and cylindrical samples (diameter 12.7 mm, thickness 1∼1.3 mm) for bulk property measurements. All samples underwent pressureless sintering under a nitrogen atmosphere using a controlled heating procedure, as depicted in Fig. 2b. The profile involved pre-drying at 130 °C for 30 min, followed by a 2-hour holding stage at 260 °C, ensuring full volatilization of organic carriers and optimal densification of the Ag network.

The sintering parameters were refined based on thermogravimetric and differential scanning calorimetry (TG-DSC) analyses (TA SDT-Q600). As presented in Fig. 3, Ag-0 exhibited sharp mass loss below 300 °C due to PEG and T evaporation, with exothermic peaks at 295 and 331 °C corresponding to thermal degradation events. In epoxy-containing formulations (Ag-1 to Ag-4), shown in Fig. 3, mass loss proceeded more gradually, and the heat flow intensity increased proportionally with resin content, indicating stronger crosslinking and slower outgassing behavior. This is further supported by Raman spectroscopy testing, where the intensity of the epoxy characteristic peak increases with increasing epoxy content after sintering, as shown in Fig. 4[39]. Final weight retention (∼85 %) confirmed the silver content, affirming the suitability of the 260 °C peak sintering temperature. This systematic preparation ensured both effective silver particle coalescence

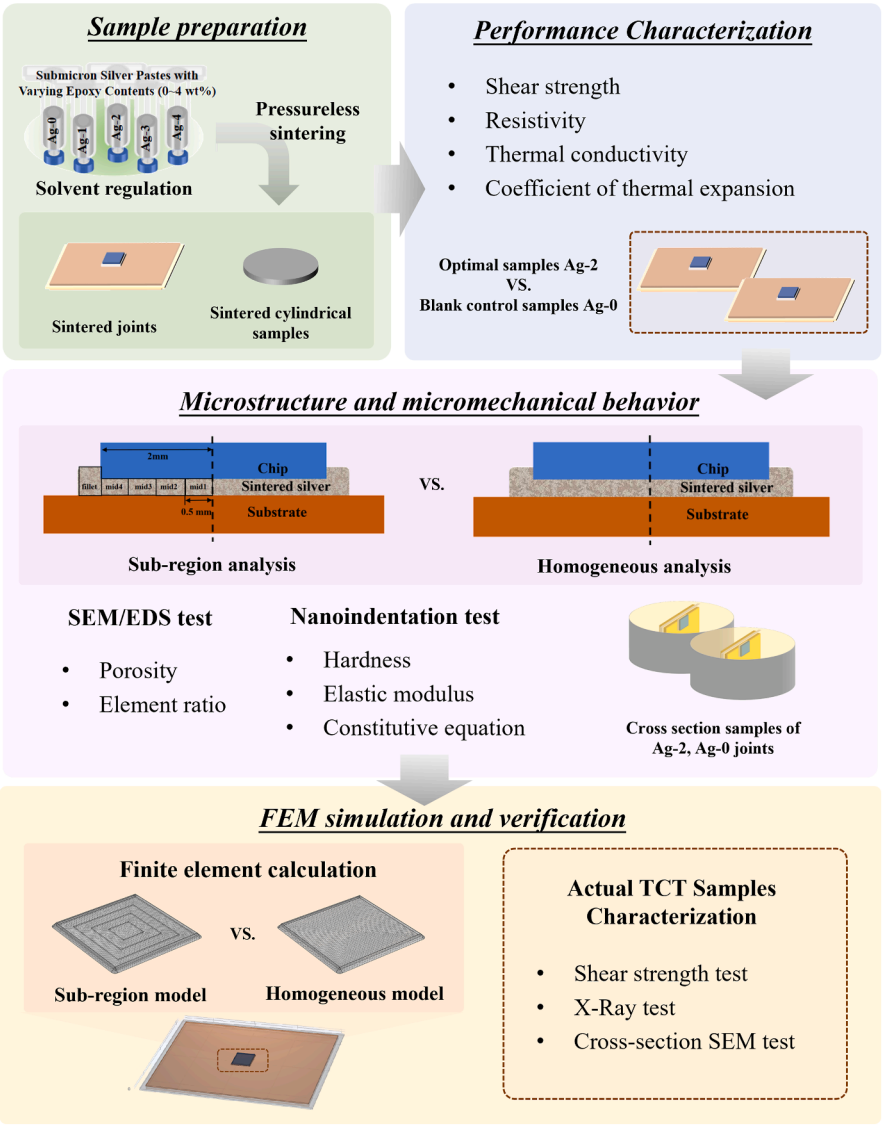

Fig. 1. Schematic illustration of the technical roadmap of this work.

and tunable organic matrix decomposition, enabling robust mechanical and electrical properties while offering a controlled platform for evaluating structure–property-processing relationships.

It is worth noting that pressureless sintering was chosen due to its tendency to produce more uneven porosity distributions compared to pressure-assisted methods, making it suitable for investigating microstructural inhomogeneity. A 4 × 4 mm^2 chip size was adopted, as it represents typical power device dimensions and provides a sufficiently large area to capture spatial variations in porosity and densification across the joint interface [16,26].

2.2. Properties evaluation

2.2.1. Shear strength

The shear strength of sintered silver joints on active metal brazing (AMB) substrates was evaluated at room temperature using a Dage 4000Plus testing system. As shown in Fig. 5, the dummy chip was sheared laterally across the bonded interface at a constant crosshead speed of 300 μm/s until mechanical failure occurred. The peak load recorded during the test was divided by the bonded area to obtain the shear strength (τ):

$$\tau = \frac{F_{max}}{A} \tag{1}$$

where F_{max} is the maximum force recorded before fracture (N), and A is the bonded area of the joint (mm^2). Each data point represents the average of at least ten measurements. Shear performance was used as a primary indicator of mechanical integrity and joint adhesion.

2.2.2. Thermal conductivity

Thermal conductivity at room temperature was assessed using an LFA 467 laser flash analyzer. Disc-shaped sintered samples were prepared with a diameter of 12.7 mm and a thickness of 1~1.3 mm. In the LFA test, a short laser pulse heats the front surface of the sample, and the temperature rise on the rear surface is recorded using an infrared detector. The thermal diffusivity (α) was derived from the time–temperature response curve. Thermal conductivity (k) was calculated using the relation:

$$k = \alpha \bullet \rho \bullet C_p \tag{2}$$

where α is thermal diffusivity, ρ is density (measured by Archimedes' method), and C_p is the specific heat capacity, referenced from standard

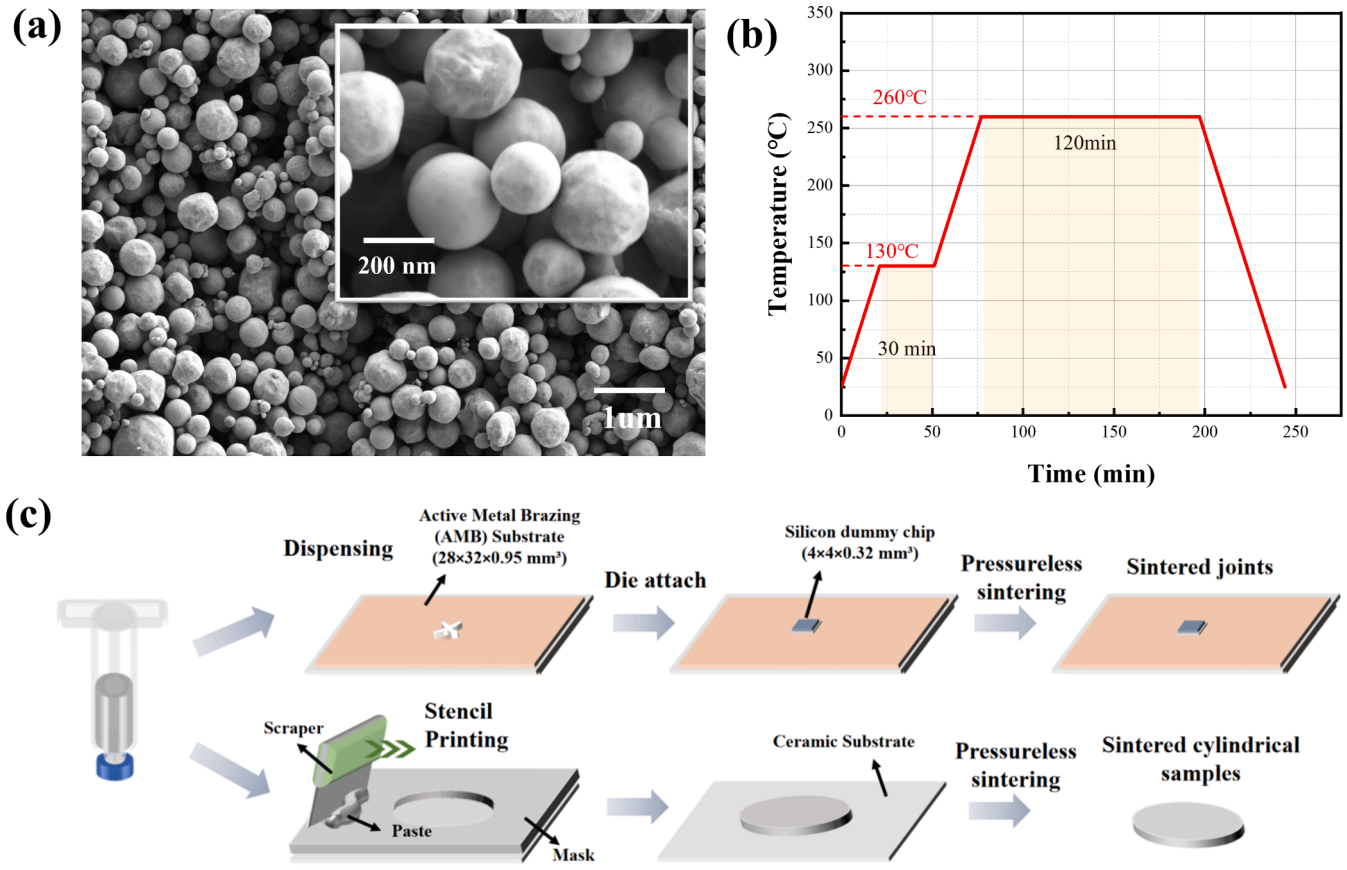

Fig. 2. (a) SEM images of spherical silver particles. (b) Pressureless sintering temperature profile. (c) Schematic diagram of the preparation process of sintered samples.

Table 1
Composition of the solvent-regulated epoxy-based Ag sintering pastes.

Pastes	Components			
	Silver particles	PEG	T	Epoxy system
Ag-0	85 wt%	10 wt%	5 wt%	0 wt%
Ag-1	85 wt%	9.33 wt%	4.67 wt%	1 wt%
Ag-2	85 wt%	8.67 wt%	4.33 wt%	2 wt%
Ag-3	85 wt%	8 wt%	4 wt%	3 wt%
Ag-4	85 wt%	7.33 wt%	3.67 wt%	4 wt%

values for silver.

2.2.3. *Electrical conductivity*

To accurately determine the electrical resistivity of sintered silver samples, an RTS-11 four-probe tester was employed. This technique minimizes the influence of contact resistance and lead resistance, making it particularly suitable for characterizing low-resistance metallic systems.

The method involves placing four collinear, equally spaced probes in direct contact with the sample surface. A known constant current (I) is supplied through the outer two probes, while the resulting voltage drop (V) is measured across the inner two probes. For thin, uniform, and

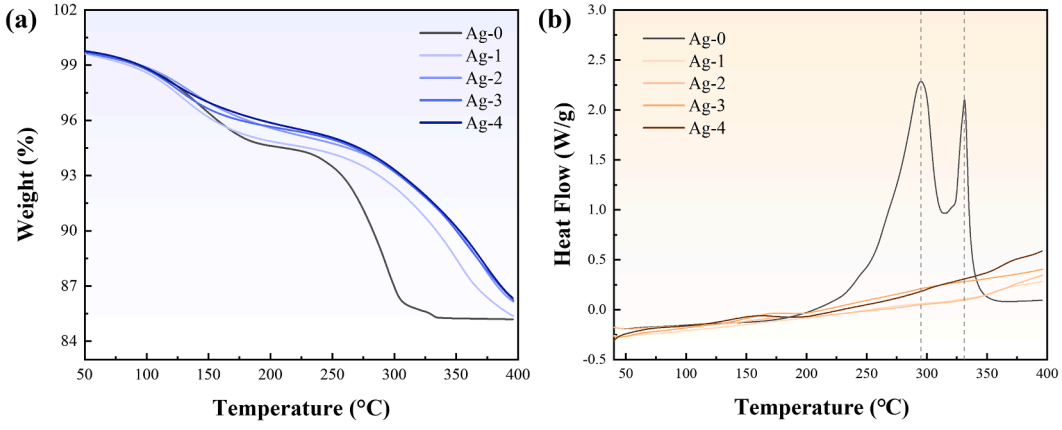

Fig. 3. Thermogravimetric analysis of silver pastes samples: (a) TG curve, (b) DSC curve.

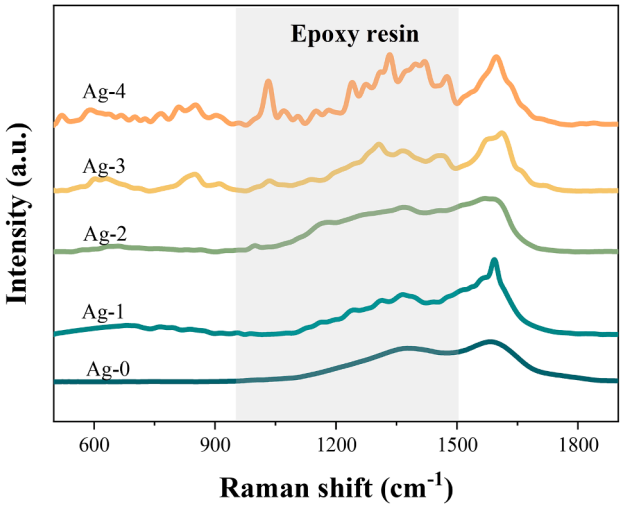

Fig. 4. Raman spectra of the silver paste samples after sintering.

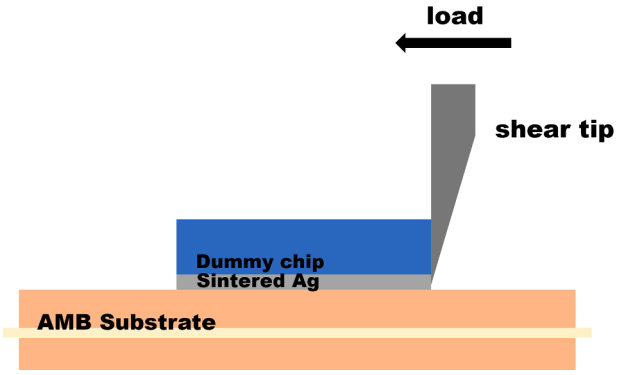

Fig. 5. Schematic of the shear strength testing setup.

planar samples, the resistivity (ρ) is calculated using the formula:

$$\rho = \frac{\pi t}{\ln 2} \cdot \frac{V}{I} \tag{3}$$

where ρ is the electrical resistivity (Ω·cm), t is the sample thickness (cm), V is the measured voltage between the inner probes (V), and I is the applied current through the outer probes (A). In practice, the measured sheet resistance is converted to conductivity ($\sigma = 1/\rho$) after accounting for thickness and geometry. Each sample was tested at multiple surface locations to ensure reproducibility, and averaged values were reported.

2.2.4. Coefficient of thermal expansion

CTE was evaluated at 200 °C using a TMA/SDTA 2 + thermal mechanical analyzer. Cylindrical specimens were subjected to linear heating from 30 °C to 250 °C at a rate of 5 °C/min. The vertical displacement (ΔL) was continuously recorded as a function of temperature, and the average CTE was calculated over the temperature range using:

$$\mathrm{CTE} = \frac{1}{L_0} \cdot \frac{dL}{dT} \tag{4}$$

where L_0 is the initial specimen length and dL/dT is the slope of the strain–temperature curve. This property is critical for evaluating compatibility with the dummy Si chips and AMB substrates under thermal cycling.

2.3. Microstructure characterization

To investigate the internal structural variations induced by epoxy modulation and thermal cycling, cross-sectional microstructure analysis was performed on these sintered joints. Samples were first sectioned perpendicular to the bonding plane using a precision low-speed diamond saw and subsequently mounted with resin, followed by fine mechanical polishing. Polished samples were ultrasonically cleaned in ethanol and then dried under vacuum.

Secondly, scanning electron microscopy (SEM, ZEISS) was used to examine the sintered joint morphology along the chip-substrate interface. To further investigate the homogeneity and residue dispersion, energy-dispersive X-ray spectroscopy (EDS) was performed under a 15 kV accelerating voltage. Quantitative maps of C, O, Ag, and other residual elements were extracted through EDS.

Then, porosity analysis was carried out using the MATLAB image processing toolbox. SEM images were converted to binary format via adaptive thresholding. The total porosity was calculated as the ratio of black (pore) pixels to total pixels within the region of interest. To analyze the pore size distribution, connected component labeling was used to segment individual pores, and the area of each pore was recorded. Finally, the pore area histogram and average pore size were derived to assess the degree of local densification.

This multi-scale microstructural mapping provided key inputs for region-resolved FEM modeling and enabled the establishment of quantitative correlations between porosity, elemental dispersion, and micromechanical performance.

2.4. Nanoindentation testing and constitutive model extraction

2.4.1. Test principle and setup

Nanoindentation testing provides a robust and localized method for evaluating the mechanical properties of materials at the nanoscale. In this study, nanoindentation measurements were carried out through the nanoindentation system (iNano, KLA Corporation) equipped with a standard diamond Berkovich indenter.

As illustrated in Fig. 6a, the test involves pressing a sharp indenter into the surface of the material with high precision. During this process, the applied load is gradually increased to a predetermined maximum and then reduced, generating a characteristic load–displacement (P–h) curve, as shown in Fig. 6b. This curve captures the material's elastic and plastic responses to the indentation load.

The analysis of the P–h curve provides insights into the mechanical behavior of the material under localized stress fields. The Oliver–Pharr method, a widely accepted analytical model, is employed to extract key mechanical parameters such as hardness and the reduced Young's modulus from the indentation data. This method enables quantitative characterization of material deformation behaviors at micro- to nanoscale resolutions.

2.4.2. Hardness and modulus

Based on the Oliver–Pharr method, the hardness (H) and reduced Young's modulus (E_r) can be derived from the load–displacement curve obtained during the nanoindentation test. The hardness is calculated using the maximum applied load (P_{max}) and the projected contact area (A_c) at the peak load, according to the following equation [40]:

$$H = \frac{P_{\max}}{A_c} \tag{5}$$

The reduced modulus E_r, which accounts for the combined elastic deformation of both the indenter and the sample, is determined from the contact stiffness (S) and the contact area as follows:

$$E_r = \frac{S\sqrt{\pi}}{2\beta\sqrt{A_c}} \tag{6}$$

Here, S is defined as the slope of the initial unloading portion of the

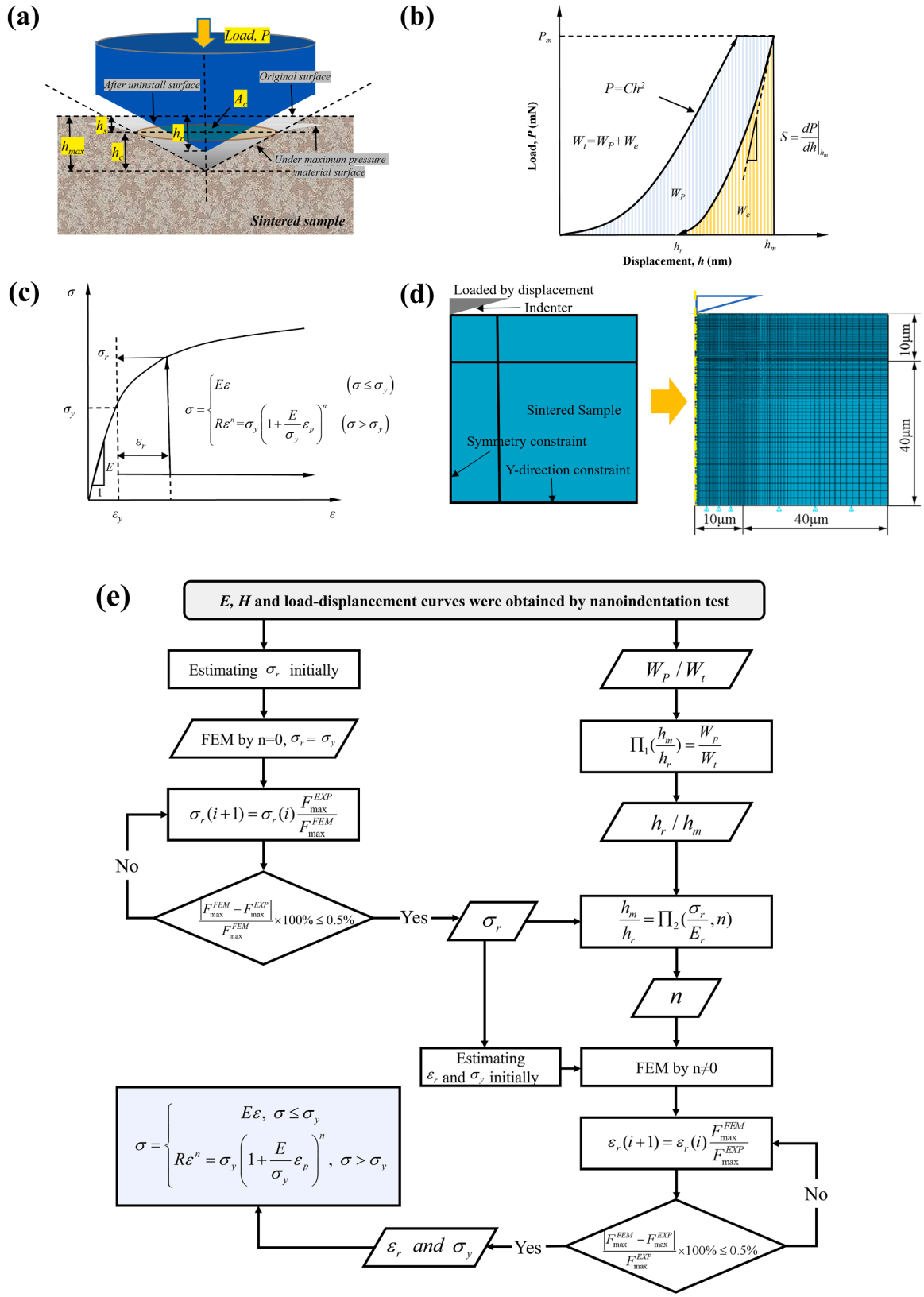

Fig. 6. (a) Schematic of the nanoindenter. (b) Typical nanoindentation curve. (c) Power-law constitutive model curve depicting the elastic–plastic behavior of metallic materials. (d) FEM of the nanoindentation test. (e) Flowchart of the inverse FEM fitting procedure used to extract region-specific constitutive parameters from nanoindentation data.

P–h curve, and β is a correction factor dependent on the geometry of the indenter. For the Berkovich indenter used in this study, $\beta = 1.034$. The projected contact area A_c is a function of the contact depth h_c, given by:

$$A_c = 24.56{h_c}^2 \tag{7}$$

The reduced modulus E_r is further related to the elastic properties of both the sample and the indenter. The relationship is expressed as [30]:

$$\frac{1}{E_r} = \frac{1-\nu^2}{E} + \frac{1-\nu_i^2}{E_i} \tag{8}$$

where E and v are the Young's modulus and Poisson's ratio of the sample, respectively, and $E_i = 1140$ GPa, $\nu_i = 0.07$ are the corresponding values for the diamond indenter. By solving Eq. (8), the actual E of the sample can be determined.

2.4.3. Power law model fitting

In nanoindentation testing, during the loading stage, the relationship between the applied load and the indentation depth can be described by Kick's model, particularly when employing a Berkovich indenter. This model is represented by a simple power-law function [30]:

$$P = \alpha h^2 \tag{9}$$

where P is the applied load, h is the indentation depth, and α is a fitting constant that reflects the elastic properties of the substrate material. This quadratic relationship enables accurate fitting of the loading segment of the load displacement (P-h) curve and provides a basis for further mechanical property extraction. In addition to the load-depth behavior, the total work of indentation W_t performed during the loading process can be partitioned into two components: the elastic work W_e and the plastic work W_p, expressed as:

$$W_t = W_e + W_p \tag{10}$$

This energy-based analysis is crucial for evaluating the plasticity and energy dissipation characteristics of the material under nanoindentation.

Furthermore, the constitutive response of metallic materials under stress can be modeled using the power-law strain hardening relationship, which characterizes the stress–strain behavior across elastic and plastic regimes. The model is defined as follows:

$$\sigma = \begin{cases} E\varepsilon, & \sigma \leqslant \sigma_y \\ R\varepsilon^n = \sigma_y\left(1 + \dfrac{E}{\sigma_y}\varepsilon_p\right)^n, & \sigma > \sigma_y \end{cases} \tag{11}$$

where σ is the applied stress, ε is the total strain, ε_p is the plastic strain, E is the Young's modulus, σ_y is the initial yield strength, R is the strength coefficient and n is the strain hardening exponent [41].

This power-law constitutive model effectively captures the nonlinear plastic deformation behavior after yielding and serves as a foundation for extracting material-specific parameters, such as yield strength and strain hardening index, through fitting of the nanoindentation data. As illustrated in Fig. 6c, this model allows for detailed interpretation of the stress–strain evolution during indentation, enhancing the understanding of the material's mechanical performance at the microscale. To resolve the elastic–plastic transition and extract constitutive parameters, an inverse finite element fitting approach is adopted. As shown in Fig. 6e, this process involves:

1. An initial estimation of the characteristic stress (σ_r) is performed by assuming a perfectly plastic model ($n = 0$) and iteratively matching the FEM-simulated maximum load with experimental data until the relative error is within 0.5 %.
2. The plastic work ratio (W_p/W_t) and indentation depth ratio (h_r/h_m) are used in a dimensional function to estimate the strain hardening exponent (n).
3. With the determined σ_r and n, characteristic strain (ε_r) and yield strength (σ_y) are iteratively optimized through parametric FEM fitting until the simulated and experimental curves match within the 0.5 % criterion.
4. The final constitutive behavior is described using a bilinear power-law model with a transition at yield, incorporating all fitted parameters into the constitutive model.

As shown in Fig. 6d, a 2D finite element model was developed using ABAQUS 2020 software to simulate the nanoindentation test process. ABAQUS software was chosen for its advanced capabilities for modeling purely mechanical problems with high computational efficiency and robust contact mechanics capabilities. The model of the sintered material part (measuring 50 μm × 50 μm) was divided into four sections to adhere to Saint-Venant's principle, thereby enhancing mesh accuracy [42,43]. In the simulation, time was expressed in seconds (s), force in millinewtons (mN), and both elastic modulus and stress were measured in megapascals (MPa). To simplify the model and improve the computational efficiency, the indenter was represented as a cone with a half-cone angle of 70.3°. Owing to its axial symmetry, the three-dimensional configuration was reduced to a two-dimensional axisymmetric model, which preserved the fidelity of the simulation results. Details of the constitutive fitting and validation procedures were reported in our previous works [35,44].

2.5. FEM simulation

Finite element simulations were performed using COMSOL Multiphysics 6.2 to investigate the mechanical behavior and stress evolution of sintered silver joints subjected to thermal cycling. COMSOL Multiphysics 6.2 was selected due to its greater flexibility in setting up coupled thermal and structural physics, particularly in handling material properties and sub-region-defined material inputs. Two modeling strategies were implemented: 1) a conventional homogeneous model and 2) a sub-region model incorporating spatially resolved material properties. The workflow of the FEM strategy is illustrated in Fig. 7a, which includes key stages of geometry definition, material parameter assignment, mesh generation, boundary condition setup, numerical solution, and post-processing analysis for comparison with TCT experimental data.

The modeled structure represents a 3D chip-sintered silver-substrate stack, as shown in Fig. 7c. The bottom of the substrate was fixed, while the top surface of the chip was constrained vertically, allowing in-plane expansion to mimic actual conditions. A temperature cycling load ranging from −55 °C to 150 °C was applied with a dwell period of 15 min at each extreme, reproducing JEDEC standard conditions (JESD22-A104D).

As shown in Fig. 7b, two modeling strategies were implemented: a conventional homogeneous model and a sub-region model incorporating spatially resolved material parameters. In the homogeneous approach, averaged mechanical properties (e.g., elastic modulus, Poisson's ratio, and CTE) were uniformly applied to the entire sintered Ag layer. In contrast, the sub-region strategy divided the joint into five distinct zones, including mid1 to mid4 and the fillet, based on SEM observations and prior reports of microstructural non-uniformity. The mid1 to mid4 regions were evenly spaced (0.5 mm intervals) along the chip horizontal direction from the joint center to the edge. The fillet, which wraps around the die periphery, was treated as a distinct region due to its susceptibility to thermal degradation. Each sub-region was assigned nanoindentation-derived modulus, hardness, and plastic constitutive parameters obtained via inverse FEM fitting. Independent meshing and boundary assignment were applied per zone to reflect mechanical transitions across the joint. This spatially refined model enabled accurate prediction of stress gradients and localization under thermal cycling, particularly near the fillet. Simulation outcomes were validated by experimental failure locations from TCT, confirming the

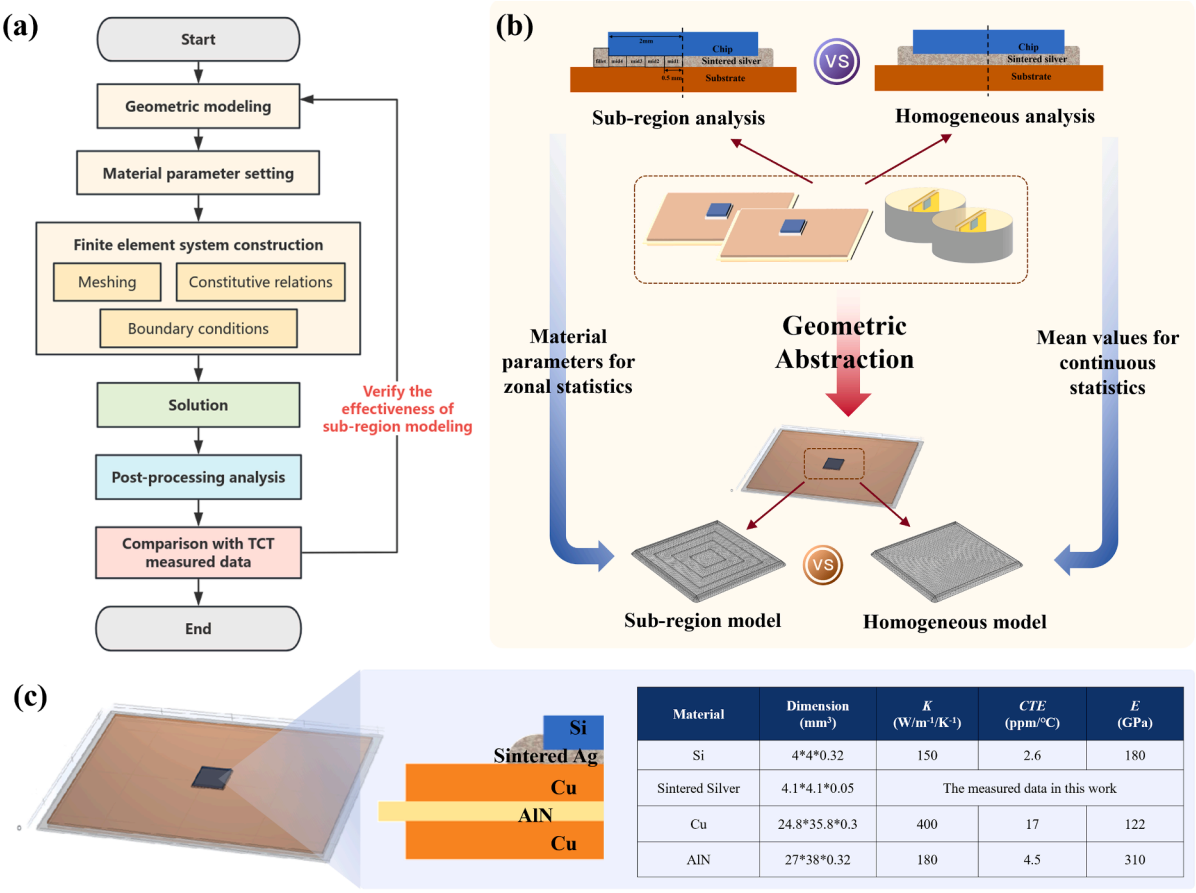

Material	Dimension (mm^3)	K ($W/m^{-1}/K^{-1}$)	CTE (ppm/°C)	E (GPa)
Si	4*4*0.32	150	2.6	180
Sintered Silver	4.1*4.1*0.05	The measured data in this work		
Cu	24.8*35.8*0.3	400	17	122
AlN	27*38*0.32	180	4.5	310

Fig. 7. (a) Workflow of the FEM strategy integrating sub-region material modeling and TCT validation. (b) Comparison of sub-region and homogeneous modeling approaches based on geometric abstraction and material parameter input. (c) Schematic of the multilayer FEM simulation model with corresponding material dimensions and properties listed.

improved fidelity of the sub-region modeling strategy. This approach provides a robust, scalable framework for simulating inhomogeneous interconnects in power electronics.

2.6. Thermal Cycling Test (TCT)

To evaluate the thermal fatigue resistance and long-term reliability of the sintered silver joints under cyclic thermal stress, TCT was conducted in accordance with JEDEC standard JESD22-A104D. Test samples were subjected to a temperature range of −55 °C to 150 °C using a programmable thermal shock chamber (VT37006S2). Each cycle consisted of a 15-minute dwell at the high and low temperature extremes, with a transition time of less than 10 min, resulting in a total of approximately 2 cycles per hour.

The total number of cycles was set to 500, and interim characterizations were performed at 250 and 500 cycles to monitor degradation evolution. At each stage, both mechanical and microstructural evaluations were carried out. Shear strength measurements were performed to assess bond integrity loss, and cross-sectional SEM imaging was used to detect internal damage such as delamination, void coalescence, and crack initiation. Surface morphologies of shear-fractured samples were examined via optical microscopy (VHX-7000, Keyence, Japan).

3. Results and discussion

3.1. Properties of the solvent-modified sintered silver materials

To identify the optimal formulation for subsequent microstructural and mechanical investigations, shear strength testing was used as the primary screening criterion due to its direct relevance to joint integrity and application reliability in power module assembly. Fig. 8 presents the average shear strength values of five sintered silver joints (Ag-0 to Ag-4) fabricated with varying epoxy contents. The results exhibit a clear parabolic trend: the strength increases with initial epoxy incorporation and then declines with excessive epoxy loading.

Specifically, Ag-0 (epoxy-free) joints displayed the lowest shear

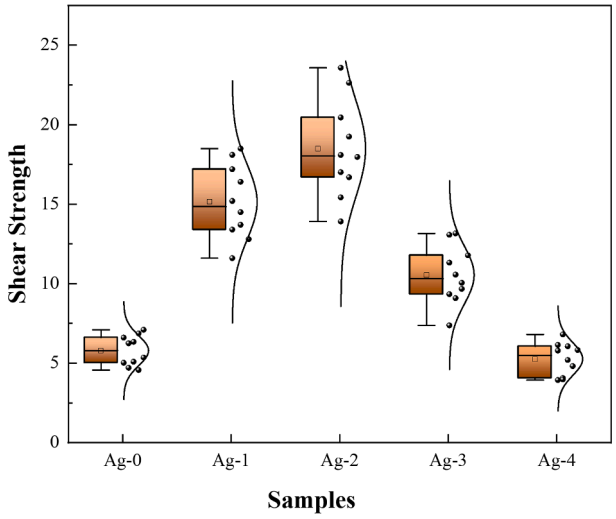

Fig. 8. Shear strength of different pressureless sintered silver joints.

strength of 5.75 MPa, reflecting limited inter-particle bonding due to high porosity and insufficient plasticity during sintering. Upon introducing 1 wt% (Ag-1) and 2 wt% (Ag-2) epoxy, the shear strength improved notably to 15.07 MPa and peaked at 18.46 MPa, respectively. This enhancement is attributed to the optimized dispersion of organic components, which improved the particle rearrangement and enhanced neck growth. As the formation and coalescence of sintering necks between adjacent silver particles, the neck growth of the sintering process was facilitated by epoxy-induced filling and stress redistribution. However, further increasing the epoxy content to 3 wt% and 4 wt% (Ag-3 and Ag-4) led to a decline in mechanical strength, likely caused by increased organic residues and pore blocking, which weakened the metallurgical bonding.

Based on the mechanical strength performance, Ag-2 was selected as the optimized sample for further in-depth analysis. Ag-0 was retained as the baseline reference to contrast the influence of epoxy regulation. The performance comparison between these two representative samples is summarized in Table 2, which shows that Ag-2 achieves a desirable balance between mechanical strength and thermal/electrical properties, maintaining acceptable resistivity (10.46 μΩ·cm), moderate thermal conductivity (29.05 $W \cdot m^{-1} \cdot K^{-1}$), and reduced CTE (13.33 ppm/°C). The electrical conductivity of Ag-2 showed about a 50 % reduction compared with the epoxy-free Ag-0, primarily due to the insulating nature of the epoxy resin. In contrast, the thermal conductivity exhibited a sharp decline, consistent with the thermal insulation characteristics of the organic addition. Though reduced thermal conductivity indeed leads to local hot spots, elevated thermal gradients, and subsequent accumulation of residual stresses to accelerate joint degradation. The selected sample (2 wt%) exhibits a thermal conductivity of 29.05 $W \cdot m^{-1} \cdot K^{-1}$ and an electrical conductivity of 10.46 μΩ/cm, which is within or exceeding an acceptable range for most high-temperature electronics packaging applications [9,37]. It is also worth mentioning that the optimization of epoxy content is essential. It is essential to carefully select and optimize the epoxy content to balance the mechanical robustness with thermal management performance in future work.

This strength-based selection not only reflects the load-bearing capability of the joint under external stress but also serves as a precursor for subsequent evaluation of microstructural uniformity, micromechanical heterogeneity, and reliability under thermal cycling, which are further explored in Sections 3.2 and 3.4.

3.2. Analysis of microstructure and micromechanical behavior

To explore the underlying mechanisms behind the observed performance differences, detailed cross-sectional characterization was conducted on Ag-0 and Ag-2 samples, focusing on porosity, elemental distribution, and micromechanical properties across five defined regions (mid1-4 and Fillet), as illustrated in Fig. 9. In addition to region-specific analysis, the averaged data across all sub-regions were also calculated to simulate conventional characterization approaches that do not resolve spatial differences. Comparisons between sub-region-resolved and average results are discussed to elucidate the added value of spatially resolved analysis in capturing microstructural and mechanical gradients.

3.2.1. Porosity

To quantitatively evaluate the effects of epoxy addition on the microstructure of the sintered silver joints, pore morphology and distribution were analyzed using SEM image processing. Based on 20 randomly selected SEM images for each sample type (four per sub-region), the average porosity of Ag-0 and Ag-2 was determined to be 32.2 % and 28.7 %, respectively. This corresponds to a 10.9 % relative reduction in porosity, attributed to the epoxy's ability to partially fill interparticle voids and promote improved densification uniformity during sintering.

Table 2
Performance comparison of solvent-modified sintered silver materials.

Properties	Samples	
	Ag-0	Ag-2
Electrical resistivity	5.37 μΩ/cm	10.46 μΩ/cm
Thermal conductivity	120.59 W/(m.K)	29.05 W/(m.K)
Thermal expansion coefficient	18.57 ppm/°C	13.33 ppm/°C

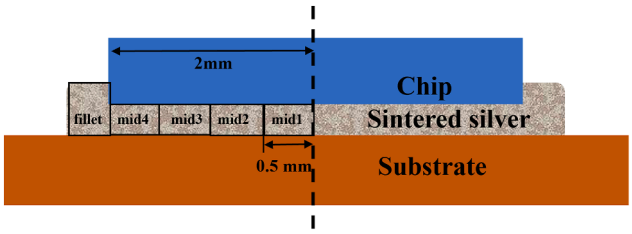

Fig. 9. Schematic illustration of the five analyzed regions (mid1–mid4 and fillet) across the sintered Ag layer.

For the sub-region strategy, porosity of the joint was measured across the designed five sub-regions (mid1 to fillet) for both Ag-0 and Ag-2 samples. As shown in Fig. 10 and Fig. 11, representative SEM images and corresponding processed binary images revealed the distinct pore structures within each region. Compared to Ag-0 with relatively large and irregular pores, Ag-2 displayed finer and more uniformly distributed pores with decreased porosity.

Fig. 12a presents the regional porosity of Ag-0, revealing clear spatial variation. The porosity values ranged from 28.21 % (mid4) to 34.17 % (mid2). This disparity (~6 %) highlighted the inhomogeneous densification typical of epoxy-free systems. By contrast, Ag-2 (Fig. 13a) exhibited much narrower variation, ranging from 26.1 % (mid1) to 30.2 % (fillet). This improved uniformity was attributed to the partial filling of interparticle voids by epoxy during sintering, which reduced localized densification gradients.

The influence of epoxy addition on pore geometry was further supported by pore size and circularity analyses. Fig. 12b and Fig. 13b illustrate the pore size distribution histograms for Ag-0 and Ag-2, respectively. Ag-0 exhibited broader distributions with more pores exceeding 2 μm^2 in area, especially in mid2 and fillet regions. In contrast, Ag-2 showed a left-shifted size distribution curve, indicating smaller, more compact pores throughout all sub-regions. Fig. 12c and Fig. 13c showed pore circularity distributions. Ag-0 featured flatter, more irregular pores (circularity < 0.4 dominating), whereas Ag-2 displayed a narrower distribution centered around 0.5~0.7, suggesting improved sphericity and sintering uniformity. Such shape regularity was advantageous for reducing stress concentration under cyclic thermal loading.

Notably, when comparing the spatially resolved porosity values with the corresponding regional average values (the rightmost bar in each bar chart), it became evident that relying only on whole-section averages hid the differences between regions. This observation underlines the importance of sub-region analysis in assessing microstructural uniformity and its relevance to reliability modeling.

3.2.2. EDS characterization

To assess the retention and dispersion of epoxy-derived species during sintering, EDS-based carbon mapping was performed across the five sub-regions of Ag-0 and Ag-2, with results summarized in Fig. 14. For the epoxy-free Ag-0, the carbon content across regions ranged narrowly between 4.4~4.8 wt%, averaging 4.6 wt%. This consistent low-level carbon signal primarily reflected residual processing artifacts and environmental contamination, exhibiting narrow spatial variation (<0.4 wt%) and negligible impact on the microstructure. In contrast, the carbon content in Ag-2 varied more substantially from 10.5 wt% (fillet)

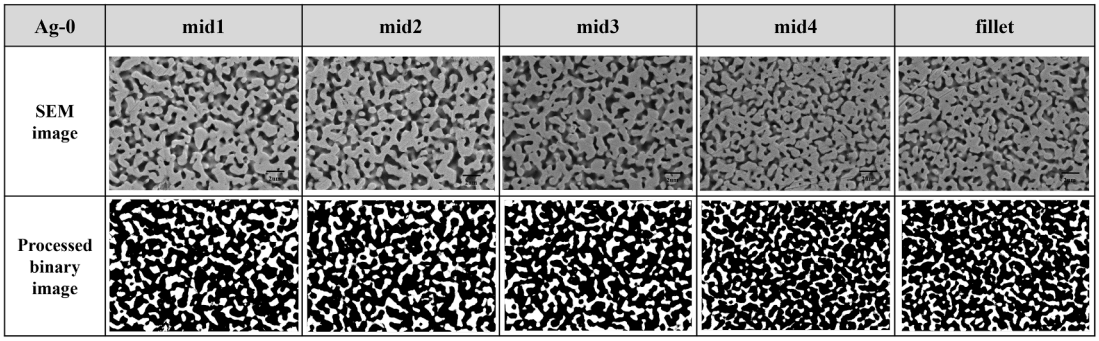

Fig. 10. Representative SEM and processed binary images of each region for Ag-0 sintered joints.

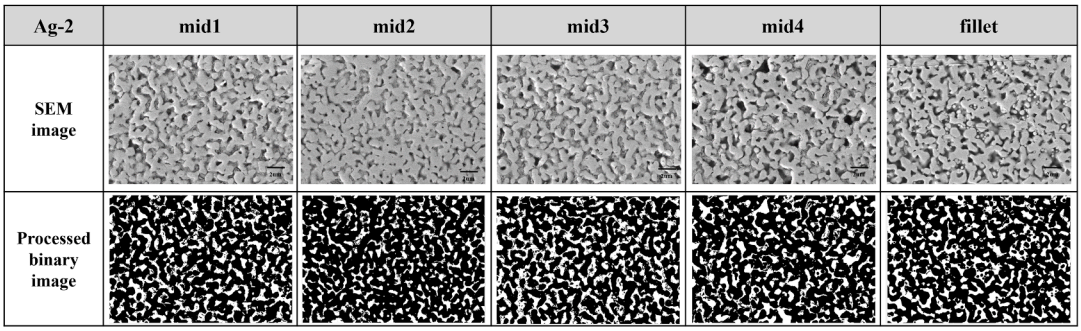

Fig. 11. Representative SEM and processed binary images of each region for Ag-2 sintered joints.

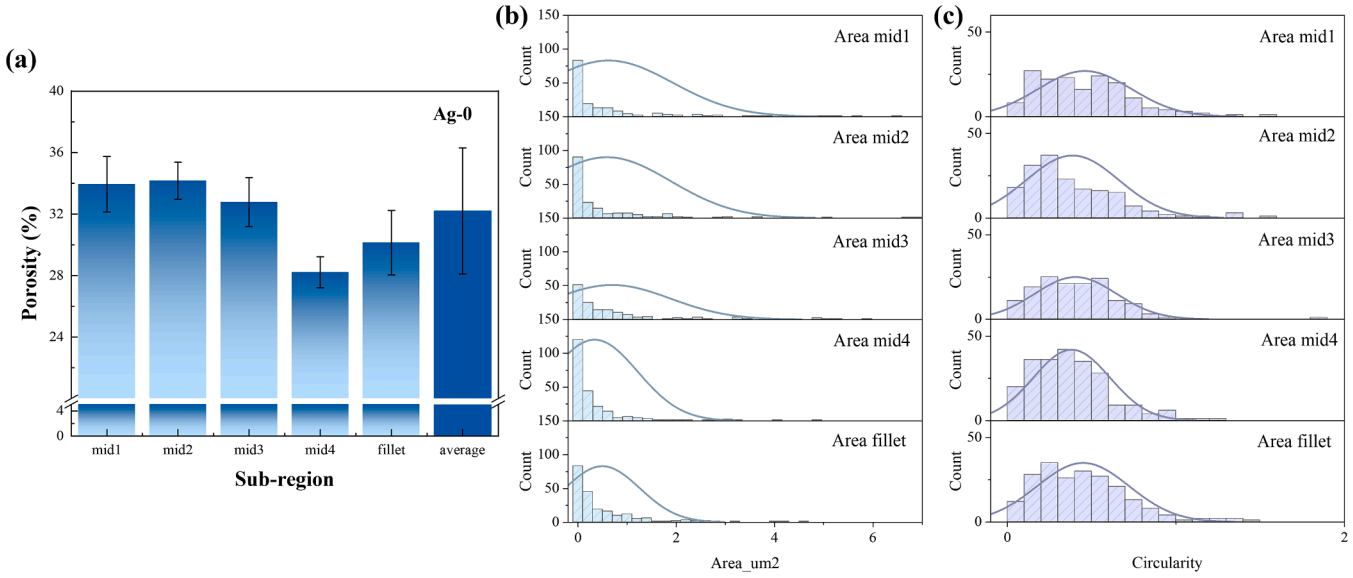

Fig. 12. (a) Regional porosity of Ag-0; (b) pore size distribution histograms; (c) pore circularity distribution across all regions.

to 12.6 wt% (mid1), with an average of 11.5 wt%. This distribution confirmed the partial retention of epoxy constituents post-sintering, especially in inner regions where gas diffusion was more restricted. Notably, the carbon level in mid1 is ~2.1 wt% above that of the fillet, suggesting a concentration gradient driven by uneven pyrolysis or volatilization during the pressureless sintering process. Despite the elevated carbon content in Ag-2, no severe adverse effects on structural integrity were observed, as evidenced by the higher mechanical performance in Section 3.1. The locally confined carbon residues may have facilitated the slight pore-filling process and promoted densification at the microscale. It is also observed that the residues did not form continuous insulating networks, which is consistent with the acceptable conductivity of Ag-2 due to the absence of resin-rich clustering or large-scale agglomeration from the non-conductive resin.

This sub-region EDS analysis further illustrated the importance of localized elemental characterization. While average carbon content provided a general indication of residual organics, only sub-region mapping revealed the spatial retention behavior of epoxy and its correlation with local porosity and densification behavior.

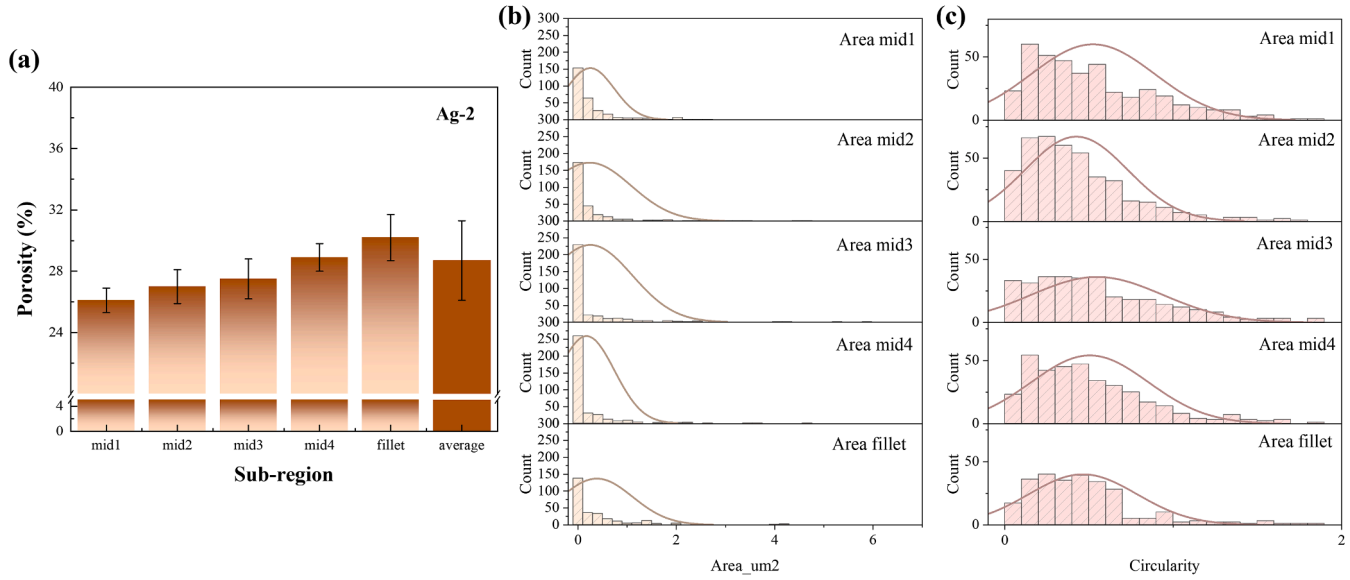

Fig. 13. (a) Regional porosity of Ag-2; (b) pore size distribution histograms; (c) pore circularity distribution across all regions.

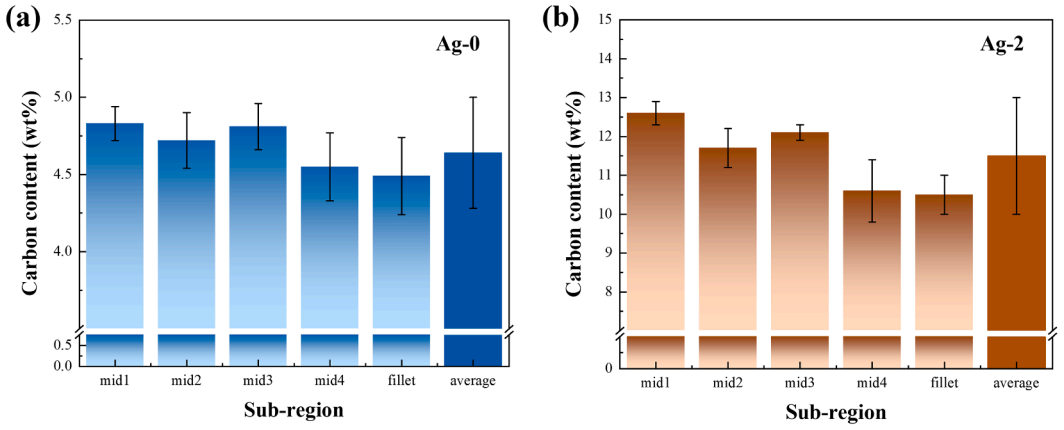

Fig. 14. EDS-based carbon content across sub-regions: (a) Ag-0; (b) Ag-2.

3.2.3. *Hardness and elastic modulus*

To evaluate the micromechanical response of sintered joints under localized stress, nanoindentation was performed across the five defined sub-regions for both Ag-0 and Ag-2 samples. The resulting hardness and elastic modulus values are presented in Fig. 15.

Ag-0 (Fig. 15a) samples exhibited relatively uniform hardness across the joint, ranging from 0.63 to 0.69 GPa, with an average of 0.65 GPa. The difference between the highest (fillet: 0.69 GPa) and lowest (mid1~mid3: 0.63 GPa) values was only ~9.5 %, indicating limited spatial variability. This suggested a more homogeneous mechanical response, albeit with higher porosity and weaker interparticle bonding. In contrast, Ag-2 (Fig. 15b) demonstrated a clear hardness gradient

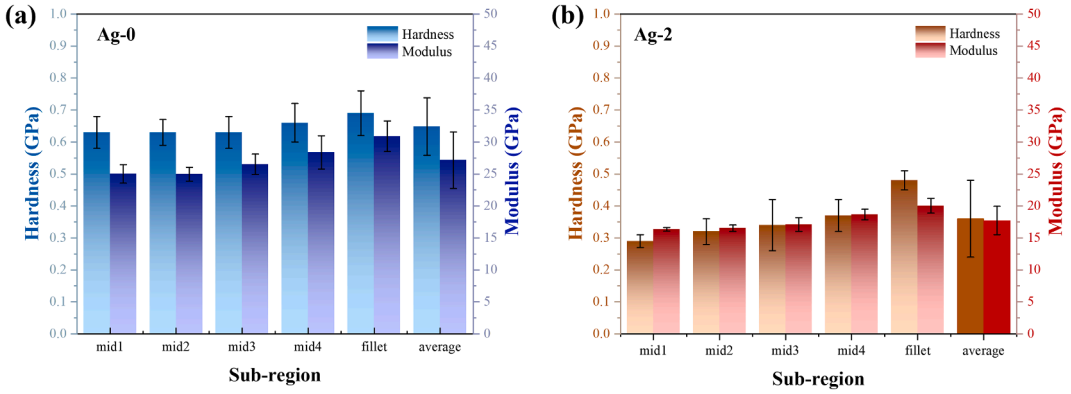

Fig. 15. Nanoindentation-derived hardness and modulus distribution across sub-regions: (a) Ag-0; (b) Ag-2.

across the joint. The hardness increased from 0.29 GPa in mid1 to 0.48 GPa in the fillet, with an average value of 0.36 GPa. The relative variation across sub-regions reached ~65 %, more than six times greater than in Ag-0. This substantial gradient highlighted the influence of epoxy on localized densification and mechanical reinforcement, particularly near the periphery where thermal stress was typically concentrated. Although the global average hardness of Ag-2 was 44.4 % lower than that of Ag-0, its localized enhancement at the joint edges helped improve resistance to crack initiation under thermal cycling. As for elastic modulus, Ag-0 samples displayed values from 24.96 to 30.89 GPa (average: 27.15 GPa), while Ag-2 samples showed a lower overall range of 16.34 to 20.03 GPa (average: 17.73 GPa). The addition of epoxy reduced the average modulus by approximately 34.7 % while redistributing mechanical stiffness from the inner regions to the outer fillet zone.

These observations emphasized that while epoxy addition reduced the overall stiffness and hardness, it introduced beneficial mechanical gradients that helped accommodate thermal expansion mismatches. For finite element simulations, using region-averaged values would overlook these critical variations, particularly in the fillet where failure tends to initiate. Therefore, sub-region-resolved mechanical input is essential to accurately simulate local stress evolution and predict failure-prone zones under thermal cycling.

3.3. Constitutive behavior

In this study, we focused on the variations in the constitutive relationships across different regions of two samples, Ag-0 and Ag-2, after partitioning them into distinct zones. Additionally, the average constitutive relationship was computed for the non-partitioned samples to facilitate a comparative analysis. This approach aims to better understand how the material's elastic–plastic behavior evolves in different regions due to partitioning, thus to further assess how it differs from the average behavior of the unpartitioned samples.

Table 3 presents the constitutive parameters for the samples. The stress–strain relationships for the selected samples are expressed using Eqs. (5) to (11), and the corresponding stress–strain curves are shown in Fig. 16.

The constitutive relationships calculated for the partitioned regions revealed that the yield strength (σ_y) was the highest in the edge regions (mid3 or mid4) of both samples. For the Ag-0 sample, the maximum yield strength reached 51.6 MPa, while for the Ag-2 sample, it peaked at 61.29 MPa. Besides, for both samples, the yield strengths in edge regions like mid3, mid4, and fillet are all at least 40 % greater than that in the central region mid1. These results suggested that the mechanical properties of the sintered samples' edge regions were superior to those of the central regions to some extent.

Moreover, for the mid3, mid4, and fillet regions, the partitioned yield strength of Ag-2 was consistently higher than that of Ag-0, possibly highlighting the influence of epoxy resin addition on the mechanical performance of the sintered samples. Notably, the maximum partitioned yield strength of Ag-0 was 2.54 times greater than its minimum partitioned yield strength, while the ratio was 4.71 for Ag-2. These variations highlighted the critical role of spatial partitioning in mechanical evaluation. As the material response differed markedly depending on the region, sub-region analysis enhanced not only the accuracy of material properties overlooked by the conventional bulk-averaged method, but also the depth of sintered die-attach materials research.

Table 3
Constitutive parameters of sintered samples.

Sample	W_p/W_t	h_r/h_m	σ_r (MPa)	n	ε_r	σ_y (MPa)
Ag-0 mid1	0.831	0.885	168.58	0.570	0.0325	20.32
Ag-0 mid2	0.823	0.871	167.80	0.497	0.0327	34.84
Ag-0 mid3	0.827	0.883	170.40	0.529	0.0326	29.30
Ag-0 mid4	0.829	0.874	173.82	0.408	0.0321	51.60
Ag-0 fillet	0.857	0.895	192.61	0.565	0.0317	24.53
Ag-0 Avg	0.832	0.876	169.08	0.504	0.0319	30.85
Ag-2 mid1	0.878	0.910	74.608	0.442	0.0310	18.38
Ag-2 mid2	0.885	0.915	78.48	0.502	0.0304	13.00
Ag-2 mid3	0.825	0.902	128.60	0.307	0.0324	61.29
Ag-2 mid4	0.832	0.906	126.79	0.335	0.0319	53.57
Ag-2 fillet	0.837	0.881	164.07	0.483	0.0332	34.49
Ag-2 Avg	0.801	0.854	92.53	0.252	0.0315	51.52

The yield strength analysis reveals marked discrepancies between averaged constitutive relationships and partitioned regions. The unpartitioned specimens "Ag-0 Avg" and "Ag-2 Avg" demonstrated respective yield strengths of 30.85 MPa and 51.52 MPa, exceeding those observed in most of their partitioned counterparts, as shown in Fig. 17. Specifically, Ag-0 Avg surpasses the mid1, mid3, and fillet regions within Ag-0 specimens; likewise, Ag-2 Avg maintained higher yield strength compared to the mid1, mid2, and fillet regions in Ag-2 specimens. These mechanical disparities underscored the inherent material heterogeneity and emphasized the criticality of localized property variations in determining global material performance.

The observed divergence between regional and bulk mechanical responses highlights two fundamental insights: First, conventional unpartitioned analysis inadequately captures critical regional property gradients that influenced operational performance. Second, the partitioning methodology provided essential spatial resolution for identifying mechanically vulnerable regions that governed failure initiation. This paradigm shifted from homogeneous assumption to inhomogeneous characterization, proving particularly crucial for performance prediction under multiaxial stress states.

Such findings substantiated the necessity of multiscale mechanical evaluation in material design. The demonstrated regional strength variations (exceeding 40 % in Ag-series specimens) necessitate a paradigm where region-specific analysis complements traditional bulk property characterization. This dual-scale approach enables more accurate failure mode prediction and optimized material utilization through targeted reinforcement strategies.

3.4. FEM simulation and verification of thermal stress during the TCT process

FEM simulations and experimental validations are employed to investigate the thermal stress behavior of Ag-0 and Ag-2 sintered joints during the TCT process. The sub-region FEM simulation provides a more detailed and accurate depiction of stress distribution compared to the homogeneous FEM simulation. The subsequent experimental validation through TCT tests and various analyses further confirms the reliability of the simulation results and emphasizes the superior thermal cycling resistance of Ag-2 sintered joints.

3.4.1. Sub-region vs homogeneous FEM simulation

The comparison between sub-region and homogeneous FEM simulations was conducted. Fig. 18 presents the homogeneous FEM simulation results of (a) Ag-0 and (b) Ag-2 sintered joints. In this figure, it is evident that the yield stress distribution in the Ag-2 sample, which has epoxy resin added after high-temperature aging, is higher than that of the Ag-0 sample without epoxy resin. This suggests that the addition of epoxy resin influences the mechanical performance of the sintered joints under high-temperature conditions.

Fig. 19 illustrates the Sub-region FEM simulation of (a) Ag-0 and (b) Ag-2 sintered joints. Compared to the results in Fig. 18, the stress distribution in the partitioned regions is more pronounced and discernible. Specifically, the stress intensity shows a clear trend of initially increasing from the center to the edge, and then decreasing, reflecting the spatial variation of mechanical properties within the samples. Furthermore, the stress intensity distribution in the partitioned Ag-2 samples reveals a generally higher value in both the sintered center and edge regions compared to the Ag-0 samples. This highlights the altered mechanical properties of the Ag-2 sample with epoxy resin after

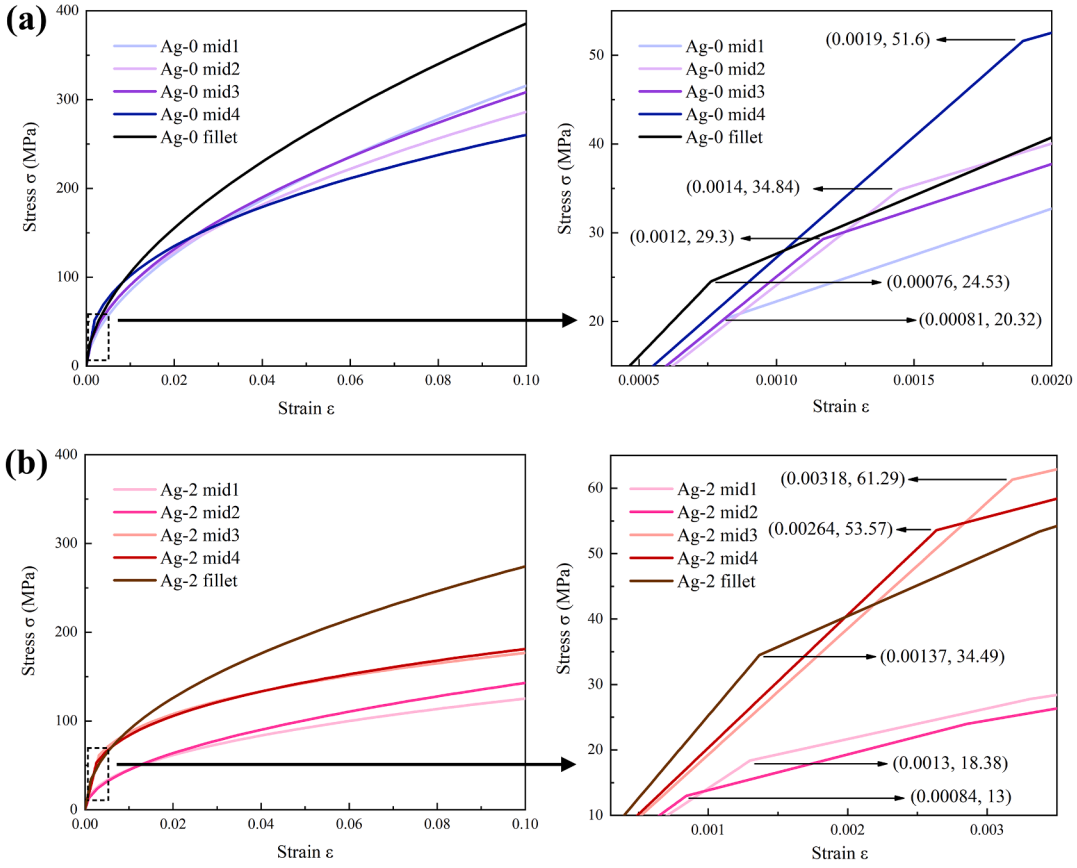

Fig. 16. Sub-region elastoplastic constitutive model of (a) Ag-0 and (b) Ag-2 sintered joints.

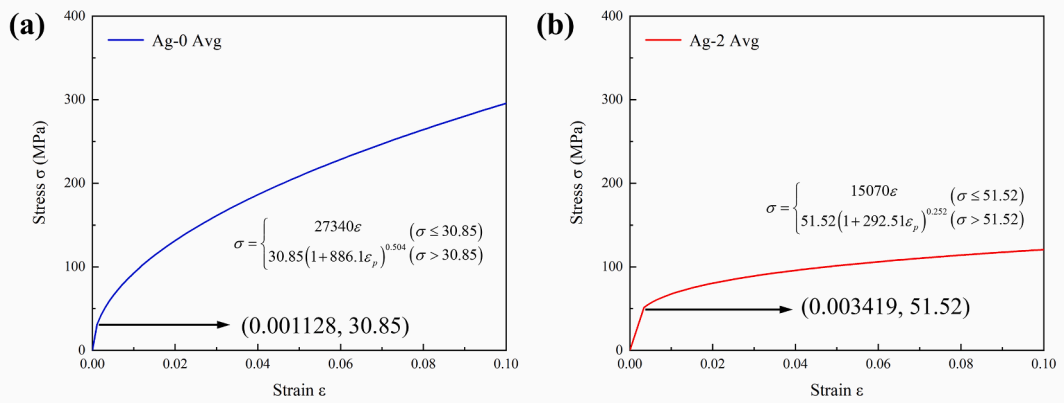

Fig. 17. Homogeneous elastoplastic constitutive model of (a) Ag-0 and (b) Ag-2 sintered joints.

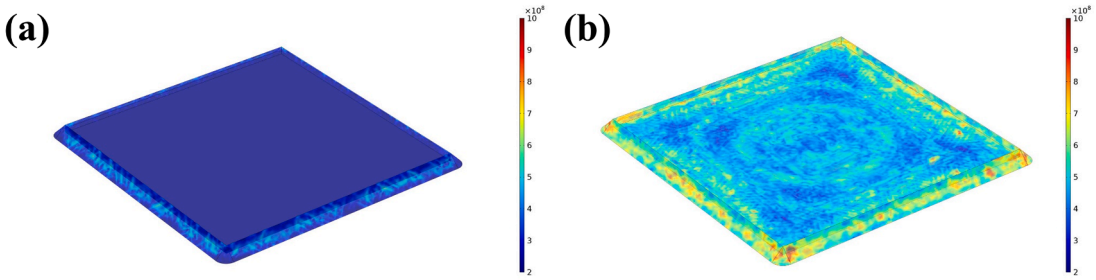

Fig. 18. Homogeneous von Mises stress(N/m^2) FEM simulation of (a) Ag-0 and (b) Ag-2 sintered joints.

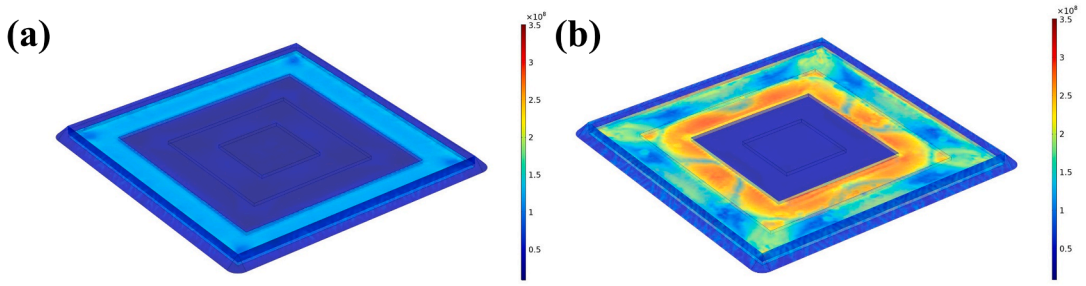

Fig. 19. Sub-region von Mises stress(N/m^2) FEM simulation of (a) Ag-0 and (b) Ag-2 sintered joints.

high-temperature aging, as compared to the Ag-0 sample without the resin.

Moreover, the use of partitioning in the FEM simulations allows for a more precise and accurate characterization of the mechanical performance, providing a clearer insight into the material's behavior across different regions. The enhanced resolution offered by sub-region analysis underscores its value in capturing local mechanical disparities that are otherwise masked in homogeneous models. This demonstrates that partitioning not only improves the clarity of the mechanical property distribution but also contributes to a more reliable assessment of the material's behavior under different conditions.

Figs. 20a and 20b showcase the average body von Mises stress over TCT test time for Ag-0 and Ag-2 sintered joints obtained from homogeneous FEM simulations in COMSOL. These figures illustrate the characteristics of stress evolution during the TCT testing process, complementing the spatial distribution insights from Figs. 18 and 19. It can be seen that the homogeneous FEM simulation results indicate a certain level of stress concentration in the Ag-2 sample compared to Ag-0, while the specific locations of stress concentration within the samples are not as clearly delineated, defined as sub-region models. Figs. 20c and 20d, which present the sub-region FEM simulation results for Ag-0 and Ag-2, offer a more detailed and precise view of stress distribution. Unlike the homogeneous model, the sub-region approach allows for the input of distinct material parameters for different regions, thereby more accurately reflecting the actual mechanical behavior of the sintered joints. The sub-region simulations reveal that the stress concentration is more prominent in specific areas, such as the transition region between the center and edge, which is a critical finding for understanding the potential failure mechanisms [20,45].

Comparison between the homogeneous and sub-region FEM results indicates that the sub-region approach offers enhanced accuracy in identifying stress concentration zones. This advantage is particularly evident in the Ag-2 sample with epoxy, where localized stress distributions captured by the sub-region model align more closely with expected failure-prone areas. In contrast, the homogeneous model may over- or underestimate stress magnitudes in specific regions, potentially

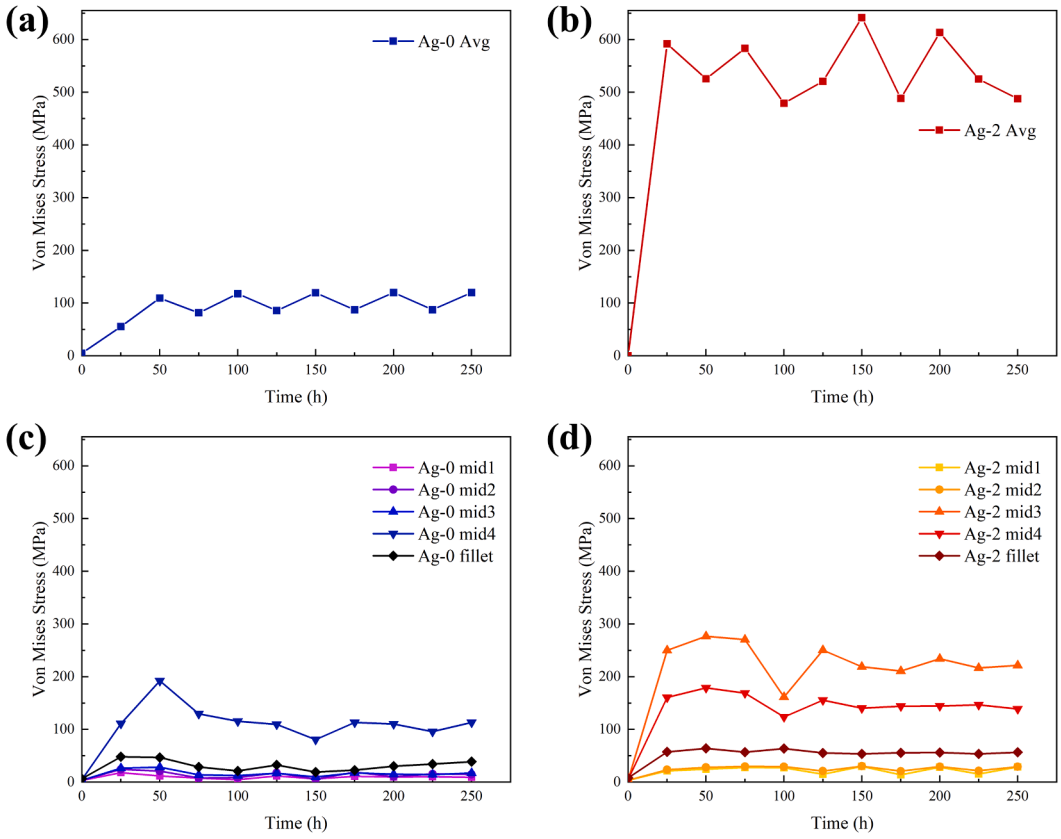

Fig. 20. Average body von Mises stress over TCT test time for homogeneous FEM simulation of (a) Ag-0 and (b) Ag-2 sintered joints and for Sub-region FEM simulation of (c) Ag-0 and (d) Ag-2 sintered joints.

resulting in misleading predictions of mechanical performance.

The data also indicate that the region between the center and edge experiences the highest stress levels, making it more susceptible to failure under adverse conditions. This finding underscores the importance of considering spatial variations in material properties when assessing the mechanical performance of sintered joints, especially those reinforced with epoxy resin.

In summary, the sub-region FEM simulations provide a more reliable and detailed characterization of stress distribution in sintered joints, highlighting the advantages of this approach over the homogeneous FEM method. The ability to input region-specific material parameters enhances the accuracy of the simulations, leading to a better understanding of the mechanical behavior of these materials under different conditions. This improved insight is crucial for the design and optimization of sintered joints, particularly in high-temperature reliability related to mechanical properties.

3.4.2. *Validation using TCT-tested samples*

To validate the FEM predictions, a series of TCT reliability tests were conducted up to 500 thermal cycles. Shear strength retention, optical microscopy, X-ray, and cross-sectional SEM analyses were performed on Ag-0 and Ag-2 samples.

The evolution of shear strength with increasing thermal cycles is shown in Fig. 21. Ag-2 consistently exhibited a higher average shear strength throughout the test, starting at 17.72 MPa and retaining 16.61 MPa after 500 cycles, corresponding to a retention rate exceeding 93 %. In contrast, Ag-0 exhibited a decline, dropping from 5.43 MPa to 4.50 MPa, reflecting a retention rate of only ~83 %. The narrower error bands of Ag-2 indicate better reproducibility and less degradation variability compared to Ag-0.

Fig. 22 presents the optical microscopy images of fracture surfaces for Ag-0 and Ag-2 joints after shear testing at different thermal cycling stages (0, 250, and 500 cycles). At the initial stage (0 cycle), both samples exhibited relatively complete and continuous fracture surfaces, indicative of uniform bonding. However, after 250 cycles, the Ag-0 interface showed pronounced color non-uniformity and evident interfacial delamination. Oxidation-induced discoloration and multi-region peeling were observed, suggesting progressive interface degradation under accumulated thermal stress. In contrast, Ag-2 maintained a more intact fracture morphology with only minor color variation and substantially reduced signs of delamination. After 500 cycles, the fracture surface of Ag-2 remained relatively clean and continuous. Although

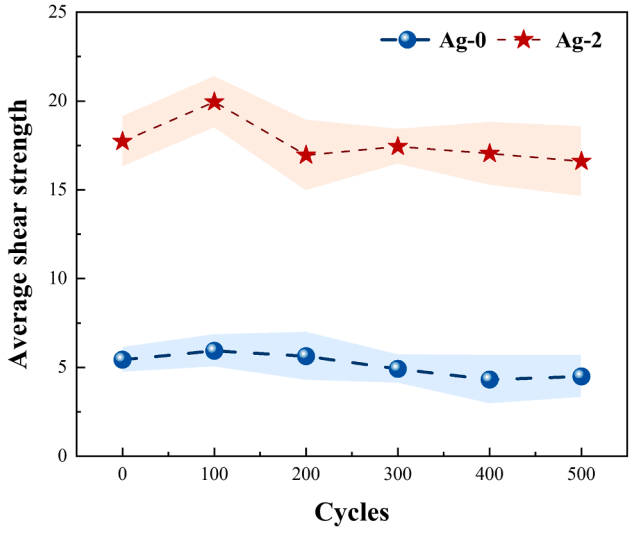

Fig. 21. Evolution of average shear strength of Ag-0 and Ag-2 sintered joints as a function of thermal cycling (up to 500 cycles). The shaded regions represent standard deviation bands.

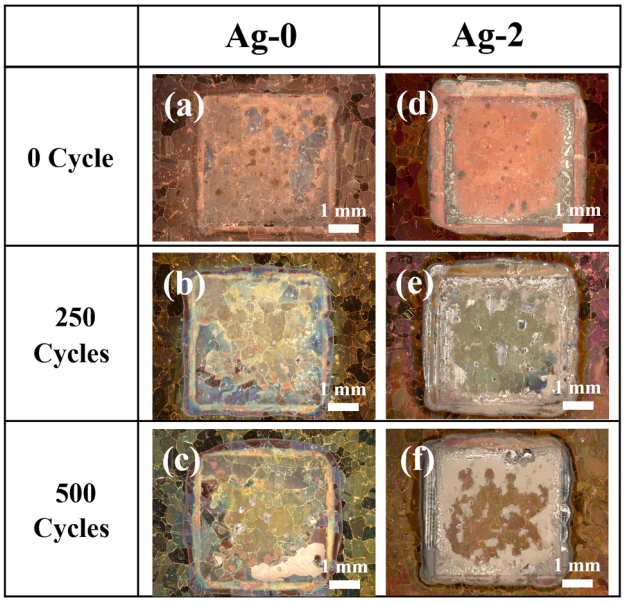

Fig. 22. Optical microscopy images of the fractured die-attach interfaces after shear testing at different thermal cycling stages: (a–c) Ag-0 samples after 0, 250, and 500 cycles; (d–f) Ag-2 samples after 0, 250, and 500 cycles.

slight discoloration was observed, the extent of interfacial damage was markedly lower than that of Ag-0, underscoring the enhanced interfacial stability and thermal fatigue resistance of the epoxy-modified Ag-2 joints.

SEM cross-sectional imaging (Fig. 23) revealed microstructural degradation mechanisms. After 500 cycles, Ag-0 samples developed obvious cracks near the fillet region (Fig. 23c), confirming failure initiation in the stress-concentrated edge predicted by simulation. Ag-2, on the other hand, maintained a dense and crack-free microstructure after cycling (Fig. 23d), which aligns with the lower localized stress differences predicted by the sub-region FEM model.

These results confirm that the sub-region modeling approach not only improves the accuracy of thermal stress predictions but also successfully correlates with experimental reliability outcomes. The superior thermal fatigue performance of Ag-2 is attributed to its more uniform mechanical profile, effective stress dispersion, and improved structural stability, which is well captured by the region-specific FEM strategy.

Future research could explore the long-term effects of thermal cycling on these sintered joints, further refining the FEM models to include time-dependent material properties. Additionally, experimental validation of the simulation results would strengthen the credibility of the findings and provide a more comprehensive understanding of the mechanical performance of sintered joints with and without epoxy resin addition.

4. Conclusions

This work presented a sub-region-based evaluation framework to investigate the structure–property-reliability relationships of epoxy-modified submicron pressureless sintered silver joints, with a focus on region-resolved mechanical modeling and thermal fatigue behavior. Through integrated experimental characterization and simulation, key conclusions are summarized as follows:

1) A material design strategy incorporating epoxy additives was adopted to modify the sintering behavior and interface quality of submicron pressureless silver pastes. Among the investigated formulations, the Ag-2 composition (with 2 wt% epoxy) was

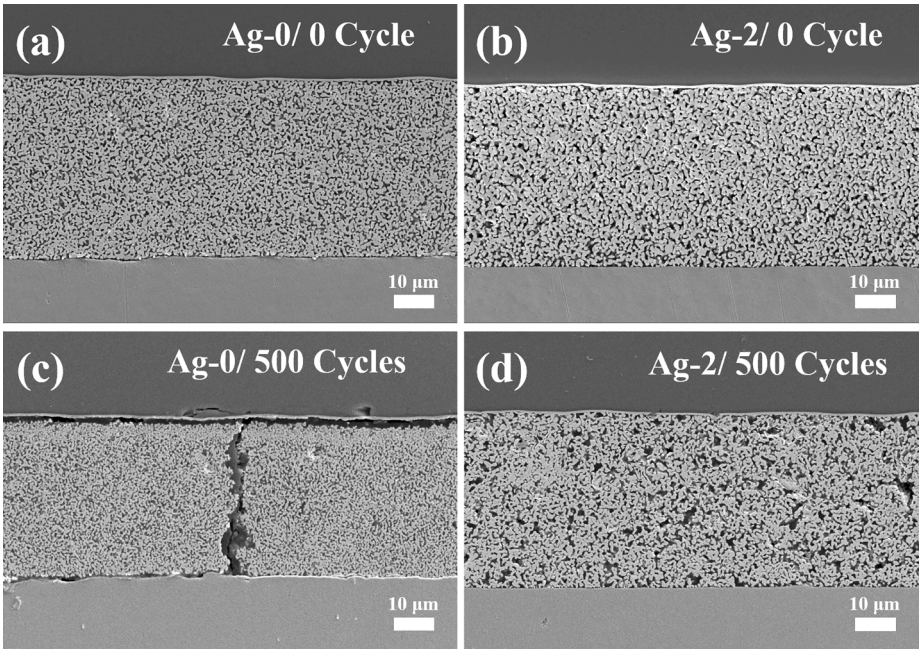

Fig. 23. SEM cross-sectional images of Ag-0 and Ag-2 sintered joints before and after 500 thermal cycles: (a, c) Ag-0 at 0 and 500 cycles; (b, d) Ag-2 at 0 and 500 cycles.

identified as optimal, offering a balanced trade-off between enhanced densification and limited residue.

2) Sub-region analysis revealed pronounced spatial variations in porosity, hardness, and modulus across the joint. The introduction of 2 wt% epoxy reduced the average porosity from 32.2 % to 28.7 % and promoted improved densification uniformity, underscoring the role of epoxy in improving microstructural consistency.
3) Region-specific FEM simulations incorporating local material properties accurately reproduced the stress distribution and failure-prone zones observed in thermal cycling experiments. Compared to homogeneous models, the sub-region simulations offered higher fidelity in predicting thermal stress evolution, especially at the joint periphery.
4) Validation through 500-cycle TCT experiments confirmed that sub-region modeling provides better agreement with failure observations than conventional homogeneous models. Ag-2 samples maintained over 80 % of initial shear strength with no apparent cracking or delamination, whereas Ag-0 joints exhibited severe interface degradation.

Overall, this work establishes a predictive, design-oriented framework linking localized micromechanical properties to the macroscopic reliability of pressureless sintered silver joints. The proposed methodology, which integrates solvent modulation, region-specific nanoindentation characterization, and finite element modeling, offers an effective strategy to manage internal inhomogeneous of interconnects in electronics packaging. The study also addressed the critical design aspects in sintered interconnect technologies, such as porosity-controlled material properties, tailored sintering profiles, and geometry-driven stress mitigation. Future studies may extend to explore multi-material interfaces, polymer-metal hybrids, and layered composite structures, where capturing and controlling local property gradients are crucial for reliability under demanding applications for electronics packaging.

CRediT authorship contribution statement

Xinyue Wang: Writing – original draft, Visualization, Project administration, Methodology, Investigation, Data curation. **Letao Bian:** Writing – original draft, Visualization, Software, Investigation, Data curation. **Zhoudong Yang:** Writing – original draft, Visualization, Formal analysis. **Haixue Chen:** Writing – original draft, Investigation, Data curation. **Yiping Sun:** Investigation, Data curation. **Wenting Liu:** Methodology, Investigation. **Guoqi Zhang:** Writing – review & editing, Supervision, Software, Conceptualization. **Jing Zhang:** Writing – review & editing, Supervision, Resources, Project administration, Conceptualization. **Pan Liu:** Writing – review & editing, Supervision, Project administration, Methodology, Funding acquisition, Conceptualization.

Declaration of competing interest

The authors declare that they have no known competing financial interests or personal relationships that could have appeared to influence the work reported in this paper.

Acknowledgments

In this work, the authors would like to thank National Natural Science Foundation of China under Grant 62304051, Shanghai Science & Technology Commission under Grant 24500790702, Zhejiang Provincial Science and Technology Program (2024C01247(SD2)), and Shanghai SiC Power Devices Engineering & Technology Research Center (19DZ2253400). Many thanks to Chat Generative Pre-Trained Transformer (ChatGPT, OpanAI) for language help.

Data availability

Data will be made available on request.

References

[1] H. Lee, V. Smet, R. Tummala, A review of SiC power module packaging technologies: Challenges, advances, and emerging issues, IEEE J. Emerging Selected Topics Power Electron. 8 (1) (2020) 239–255, https://doi.org/10.1109/jestpe.2019.2951801.
[2] B. Shi, A.I. Ramones, Y. Liu, H. Wang, Y. Li, S. Pischinger, J. Andert, A review of silicon carbide MOSFETs in electrified vehicles: Application, challenges, and future development, IET Power Electron. 16 (12) (2023) 2103–2120, https://doi.org/10.1049/pel2.12524.

[3] S.L. Zhao, Y. Tong, C.B. Wang, E.R. Yao, Challenges and progress in packaging materials for power modules with high operation temperature: Review, J. Mater. Sci.-Mater. Electron. 35 (35) (2024) 30, https://doi.org/10.1007/s10854-024-14002-4.
[4] T.F. Chen, K.S. Siow, Comparing the mechanical and thermal-electrical properties of sintered copper (Cu) and sintered silver (Ag) joints, J. Alloy. Compd. 866 (2021), https://doi.org/10.1016/j.jallcom.2021.158783.
[5] Z. Cui, Q. Jia, H. Zhang, Y. Wang, L. Ma, G. Zou, F. Guo, Review on shear strength and reliability of nanoparticle sintered joints for power electronics packaging, J. Electron. Mater. 53 (6) (2024) 2703–2726, https://doi.org/10.1007/s11664-024-10970-9.
[6] V.R. Manikam, C. Kuan Yew, Die attach materials for high temperature applications: A review, IEEE Trans. Comp. Packaging Manuf. Technol. 1 (4) (2011) 457–478, https://doi.org/10.1109/tcpmt.2010.2100432.
[7] S.A. Paknejad, S.H. Mannan, Review of silver nanoparticle based die attach materials for high power/temperature applications, Microelectron. Reliab. 70 (2017) 1–11, https://doi.org/10.1016/j.microrel.2017.01.010.
[8] P. Peng, A. Hu, A.P. Gerlich, G. Zou, L. Liu, Y.N. Zhou, Joining of eratures: Processes properties, and applications, ACS Appl. Mater. Interfaces 7 (23) (2015) 12597–12618, https://doi.org/10.1021/acsami.5b02134.
[9] H. Zhang, J. Minter, N.-C. Lee, A brief review on high-temperature, Pb-free die-attach materials, J. Electron. Mater. 48 (1) (2018) 201–210, https://doi.org/10.1007/s11664-018-6707-6.
[10] P. Zhang, X. Jiang, P. Yuan, H. Yan, D. Yang, Silver nanopaste: Synthesis, reinforcements and application, Int. J. Heat Mass Transf. 127 (2018) 1048–1069, https://doi.org/10.1016/j.ijheatmasstransfer.2018.06.083.
[11] Y. Gao, W. Li, C. Chen, H. Zhang, J. Jiu, C.-F. Li, S. Nagao, K. Suganuma, Novel copper particle paste with self-reduction and self-protection characteristics for die attachment of power semiconductor under a nitrogen atmosphere, Mater. Des. 160 (2018) 1265–1272, https://doi.org/10.1016/j.matdes.2018.11.003.
[12] Y. Chang, X. Yao, Y. Chen, L. Huang, D. Zou, Review on ceramic-based composite phase change materials: Preparation, characterization and application, Compos. Part B: Eng. 254 (2023), https://doi.org/10.1016/j.compositesb.2023.110584.
[13] X. Wang, Z. Yang, L. Ji, Z. Zeng, H. Chen, J. Fan, J. Zhang, P. Liu. An SEM-based finite element analysis of Cu-Ag sintered joints on thermal shock reliability, 2024, IEEE, Tianjin, China, 2024, https://doi.org/10.1109/ICEPT63120.2024.10668475.
[14] X. Huang, Y. Wang, Q. Zhu, Z. Du, L. Zhou, H. Liu, Thermal creep and fatigue failure of the sintered silver solder in a SiC-IGBT module under power cycling, Eng. Fail. Anal. 154 (2023), https://doi.org/10.1016/j.engfailanal.2023.107625.
[15] Z. Peng, Y. Li, Y. Rao, X. Zhao, Z. Liang, X. Yang, Effect of thermal cycling on microstructure and mechanical properties of nano-silver microsolder joint, Microelectron. Reliab. 164 (2025), https://doi.org/10.1016/j.microrel.2024.115566.
[16] G. Chang, D. An, E. Deng, X. Li, H. Luo, Y. Huang, Research on the key processes of large-area silver sintering for SiC power modules, IEEE Trans. Compon. Packag. Manuf. Technol. 15 (2) (2025) 410–420, https://doi.org/10.1109/tcpmt.2025.3531127.
[17] L. Mikutta, F. Otto, J. Schadewald, On the influence of the porosity and homogeneity of sintered die-attach layers on the power cycling performance, Microelectron. Reliab. 168 (2025), https://doi.org/10.1016/j.microrel.2025.115691.
[18] L. Yin, F. Yang, X. Bao, W. Xue, Z. Du, X. Wang, J. Cheng, H. Ji, J. Sui, X. Liu, Y. Wang, F. Cao, J. Mao, M. Li, Z. Ren, Q. Zhang, Low-temperature sintering of Ag nanoparticles for high-performance thermoelectric module design, Nat. Energy 8 (7) (2023) 665–674, https://doi.org/10.1038/s41560-023-01245-4.
[19] X. Wang, H. Chen, Z. Yang, J. Zhang, G. Zhang, P. Liu, Finite Element Analysis and Experimental Investigation of Die-Attach Fillet Influence on the Reliability of Epoxy-Based Pressure-Less Sintered Silver Joints, 2025 26th International Conference on Thermal, Mechanical and Multi-Physics Simulation and Experiments in Microelectronics and Microsystems, (EuroSimE) (2025) 1–7, https://doi.org/10.1109/EuroSimE65125.2025.11006635.
[20] D. He, D. Huang, D. Jiang, Modeling and studies of fracture in functionally graded materials under thermal shock loading using peridynamics, Theor. Appl. Fract. Mech. 111 (2021), https://doi.org/10.1016/j.tafmec.2020.102852.
[21] W. Liu, X. Wang, J. Zhang, G. Zhang, C. Chen, P. Liu, Quartet structure generation set algorithm based 3D reconstruction on porous structures of sintered copper joints for power electronics packaging, Scr. Mater. 265 (2025), https://doi.org/10.1016/j.scriptamat.2025.116750.
[22] T. Wang, L. Xu, P. Zhu, T. Zhao, R. Sun, Ieee, Simulation of performance and reliability of nano-copper paste in power device packaging, 24th International Conference on Electronic Packaging Technology (ICEPT), Shihezi, Peoples R China, 2023. https://doi.org/10.1109/ICEPT59018.2023.10492164.
[23] D. Kim, C. Chen, A. Suetake, C. Choe, T. Sugahara, S. Nagao, K. Suganuma, Development of thermal shock-resistant of GaN/DBC die-attached module by using Ag sinter paste and thermal stress relaxation structure, Microelectron. Reliab. 88–90 (2018) 779–787, https://doi.org/10.1016/j.microrel.2018.07.044.
[24] Y. Li, P. Wang, J. Li, H. Long, R. Yao, X. Wang, H. Li, Ieee, Electro-thermal stress comparison between full pressure and silver sintered package press pack IGBT, IEEE 10th International Symposium on Power Electronics for distributed Generation Systems (PEDG), Peoples R China, Xian, 2019, pp. 7–12. https://doi.org/10.1109/PEDG.2019.8807496.
[25] T. Sato, Y. Kariya, H. Takahashi, T. Nakamura, Y. Aiko, Evaluation of fatigue crack propagation behavior of pressurized sintered Ag nanoparticles and its application to thermal fatigue life prediction of sintered joint, Mater. Trans. 60 (6) (2019) 850–857, https://doi.org/10.2320/matertrans.MH201802.
[26] J. Xue, X. Li, High-pressure-assisted large-area sintered-silver substrate bonding for SiC power module packaging, Materials 17 (8) (2024), https://doi.org/10.3390/ma17081911.
[27] F. Khodabakhshi, M. Zareghomsheh, G. Khatibi, Nanoindentation creep properties of lead-free nanocomposite solders reinforced by modified carbon nanotubes, Mater. Sci. Eng. A 797 (2020), https://doi.org/10.1016/j.msea.2020.140203.
[28] R. Goodall, T.W. Clyne, A critical appraisal of the extraction of creep parameters from nanoindentation data obtained at room temperature, Acta Mater. 54 (20) (2006) 5489–5499, https://doi.org/10.1016/j.actamat.2006.07.020.
[29] J. Fan, D. Jiang, H. Zhang, D. Hu, X. Liu, X. Fan, G. Zhang, High-temperature nanoindentation characterization of sintered nano-copper particles used in high power electronics packaging, Results Phys. 33 (2022), https://doi.org/10.1016/j.rinp.2021.105168.
[30] J. Wang, C. Yang, Y. Liu, Y. Li, Y. Xiong, Using nanoindentation to characterize the mechanical and creep properties of shale: Load and loading strain rate effects, ACS Omega 7 (16) (2022) 14317–14331, https://doi.org/10.1021/acsomega.2c01190.
[31] W. Chen, X. Liu, D. Hu, X. Liu, X. Zhu, X. Fan, G. Zhang, J. Fan, Unraveling the hydrogen sulfide aging mechanism on electrical-thermal–mechanical property degradation of sintered nanocopper interconnects used in power electronics packaging, Mater. Des. 238 (2024), https://doi.org/10.1016/j.matdes.2024.112702.
[32] W. Chen, X. Liu, Z. Yang, D. Hu, X. Liu, X. Zhu, X. Fan, G. Zhang, J. Fan, Insights into sulfur and hydrogen sulfide induced corrosion of sintered nanocopper paste: A combined experimental and ab initio study, Mater. Des. 240 (2024), https://doi.org/10.1016/j.matdes.2024.112876.
[33] S. Heuer, B.S. Li, D.E.J. Armstrong, Y. Zayachuk, C. Linsmeier, Microstructural and micromechanical assessment of aged ultra-fast sintered functionally graded iron/tungsten composites, Mater. Des. 191 (2020), https://doi.org/10.1016/j.matdes.2020.108652.
[34] A. Wijaya, B. Eichinger, F.F. Chamasemani, B. Sartory, R. Hammer, V. Maier-Kiener, D. Kiener, M. Mischitz, R. Brunner, Multi-method characterization approach to facilitate a strategy to design mechanical and electrical properties of sintered copper, Mater. Des. 197 (2021), https://doi.org/10.1016/j.matdes.2020.109188.
[35] X. Wang, H. Chen, Z. Yang, W. Liu, Z. Zeng, G. Zhang, J. Zhang, J. Fan, P. Liu, Microstructure evolution and micromechanical behavior of solvent-modified Cu–Ag composite sintered joints for power electronics packaging at high temperatures, J. Mater. Res. Technol. 30 (2024) 8433–8450, https://doi.org/10.1016/j.jmrt.2024.05.196.
[36] X. Wang, Z. Yang, B. Wang, W. Chen, G. Zhang, J. Zhang, J. Fan, P. Liu, Effect of epoxy resin addition on properties and corrosion behavior of sintered joints in power modules serviced offshore, J. Mater. Res. Technol. 25 (2023) 6593–6612, https://doi.org/10.1016/j.jmrt.2023.07.098.
[37] X. Wang, Z. Zeng, G. Zhang, J. Zhang, P. Liu, Joint analysis and reliability test of epoxy-based nano silver paste under different pressure-less sintering processes, J. Electron. Packag. 144 (4) (2022), https://doi.org/10.1115/1.4053432.
[38] B.-U. Hwang, K.-H. Jung, K.D. Min, C.-J. Lee, S.-B. Jung, Pressureless Cu–Cu bonding using hybrid Cu–epoxy paste and its reliability, J. Mater. Sci. Mater. Electron. 32 (3) (2021) 3054–3065, https://doi.org/10.1007/s10854-020-05055-2.
[39] A. Al Soud, S.I. Daradkeh, A. Knápek, V. Holcman, D. Sobola, Electrical characteristics of different concentration of silica nanoparticles embedded in epoxy resin, Phys. Scr. 98 (12) (2023), https://doi.org/10.1088/1402-4896/ad070c.
[40] W.C. Oliver, G.M. Pharr, An improved technique for determining hardness and elastic modulus using load and displacement sensing indentation experiments, J. Mater. Res. 7 (6) (2011) 1564–1583, https://doi.org/10.1557/jmr.1992.1564.
[41] J. Luo, J. Lin, A study on the determination of plastic properties of metals by instrumented indentation using two sharp indenters, Int. J. Solids Struct. 44 (18–19) (2007) 5803–5817, https://doi.org/10.1016/j.ijsolstr.2007.01.029.
[42] D.I. Zhuk, M.G. Isaenkova, Y.A. Perlovich, O.A. Krymskaya, Finite element simulation of microindentation, Russian Metallurgy (metally) 2017 (5) (2017) 390–396, https://doi.org/10.1134/s0036029517050123.
[43] Y.-T. Cheng, C.-M. Cheng, Scaling, dimensional analysis, and indentation measurements, Mater. Sci. Eng.: R: Rep. 44 (4–5) (2004) 91–149, https://doi.org/10.1016/j.mser.2004.05.001.
[44] H. Chen, X. Wang, Z. Zeng, G. Zhang, J. Zhang, P. Liu, Solvent modulation, microstructure evaluation, process optimization, and nanoindentation analysis of micro-Cu@Ag core–shell sintering paste for power electronics packaging, J. Mater. Sci. Mater. Electron. 34 (24) (2023), https://doi.org/10.1007/s10854-023-11083-5.
[45] Y. Wang, C. Wang, Y. You, W. Cheng, M. Dong, Z. Zhu, J. Liu, L. Wang, X. Zhang, Y. Wang, Thermal stress analysis of optimized functionally graded coatings during crack propagation based on finite element simulation, Surf. Coat. Technol. 463 (2023), https://doi.org/10.1016/j.surfcoat.2023.129535.